

NATIONAL RADIO ASTRONOMY OBSERVATORY
Charlottesville, Virginia

ELECTRONICS DIVISION INTERNAL REPORT NO. 330

A Model for Phased Array Feed

D. Anish Roshi¹, J. Richard Fisher¹

¹ National Radio Astronomy Observatory, Charlottesville,

January 27, 2016

A Model for Phased Array Feed

D. Anish Roshi & J. Richard Fisher

January 27, 2016

Version 2.0

Abstract

In this report we present a model for phased array feed (PAF) and compare the model predictions with measurements. A theory for loss-less PAF is presented first. To develop the theory we ask the question – what is the best T_{sys}/η_{ap} that can be achieved when a PAF is used on a telescope to observe a source at an angle θ_s, ϕ_s from the boresight direction ? We show that a characteristic matrix for the *system* (i.e. PAF+telescope+receiver) can be constructed starting from the signal-to-noise ratio of the observations and the best T_{sys}/η_{ap} can be obtained from the maximum eigenvalue of the characteristic matrix. For constructing the characteristic matrix, we derive the open-circuit voltage at the output of the antenna elements in the PAF due to (a) radiation from source, (b) radiation from ground (spillover), (c) radiation from sky background and (d) noise due to the receiver. The characteristic matrix is then obtained from the correlation matrices of these voltages. We then describe a modeling program developed to implement the theory presented here. Finally the model predictions are compared with results from test observations made toward Virgo A with a prototype PAF (Kite array) on the GBT[1]. The main features of the model and summary of the comparison are :

- We present an *ab initio* model for the PAF. The model is developed from Lorentz Reciprocity theorem (see Section 3.3), which is derived from Maxwell's equation with no further assumptions made, and also with the aid of first and second law of thermodynamics (see Appendices). The result of the model is presented as a theorem (see Section 3).
- Based on the model results, we show that the receiver temperature of the PAF can be expressed as a generalization of the equation for a single antenna followed by a receiver. The proof of this statement is given in Appendix F.
- The model well predicts the measured $\frac{T_{sys}}{\eta}$ vs offset angle from boresight direction but needs an increase in receiver temperature of about 5K to match the measured results ¹. The model also predicts the measured $\frac{T_{sys}}{\eta}$ vs frequency with the additional increase in receiver temperature mentioned above.
- The aperture and spillover efficiencies obtained from the best fit model are 65% and 98% respectively between 1.3 and 1.7 GHz.

¹In Roshi et al. (2015)[1]), we presented our preliminary model results, where the excess temperature needed is given as 8 K. Our improved model (see Section 5) requires only 5K excess noise. Also the aperture efficiency given in [1] is 70 %, which has been revised to 65% in this report.

1 Introduction

Feeds consisting of dense, electrically small antenna arrays, referred to as Phased Array Feed (PAF), are now of significant interest [2, 3, 4, 5]. These dense arrays sample the focal field pattern of the telescope. Multiple beams are then formed by combining the signals sampled by the array elements with complex weights that form an efficient reflector illumination. The beams formed using a PAF can fully sample the FOV. Additionally, a PAF can be used to improve spillover efficiency as well as the illumination of the dish. However, mutual coupling between array elements are a major hurdle in designing a PAF. Mutual coupling modifies the element radiation patterns. It also couples amplifier noise. Therefore, detailed electromagnetic, noise and network modeling is needed to design a PAF for radio astronomy applications [6].

Several research groups have analyzed and modeled the noise performance[7, 8], electromagnetic properties of PAFs[9, 10] and signal processing aspects[11]. In this report, we present details of a new PAF model developed at NRAO starting from Lorentz Reciprocity theorem (see Section 3.3), and also with the aid of first and second law of thermodynamics (see Appendices). The implementation of the theory using a matlab program is discussed in Section 4. The model predictions are compared with measurements in Section 5.

2 Some basic Assumptions and Approximations

The following assumptions and approximations are made during the development of the model.

- The PAF is assumed to be loss-less and reciprocal device. This assumption implies a symmetry in the impedance matrix of PAF, *viz*, $z_{ij} = z_{ji}$, where z_{ij} are the elements of the impedance matrix.
- The parabolic reflector and ground are assumed to be located at the far-field of PAF. We also neglect scattering at the edge of the reflector and in any mounting structure.
- The fields on the aperture of the antenna are computed using geometric optics approximations.
- The amplifier noise radiated from the PAF is not reflected back to the system.

3 Theory of loss-less Phased Array Feed

The performance of PAF is usually expressed as the ratio of the system temperature by aperture efficiency (T_{sys}/η_{ap})² To develop the theory we ask the question :

“For a PAF installed on a telescope what is the minimum value of T_{sys}/η_{ap} that can be obtained when observing a compact source (point source) at angle (θ_s, ϕ_s) from the boresight direction ?”

The answer to this question is the following theorem:

²The directly measurable quantity is the ratio $\frac{T_{sys}}{\eta_{ap}\eta_{rad}}$, where η_{rad} is the radiation efficiency of the PAF. In this report we are considering a loss-less PAF and hence $\eta_{rad} = 1$.

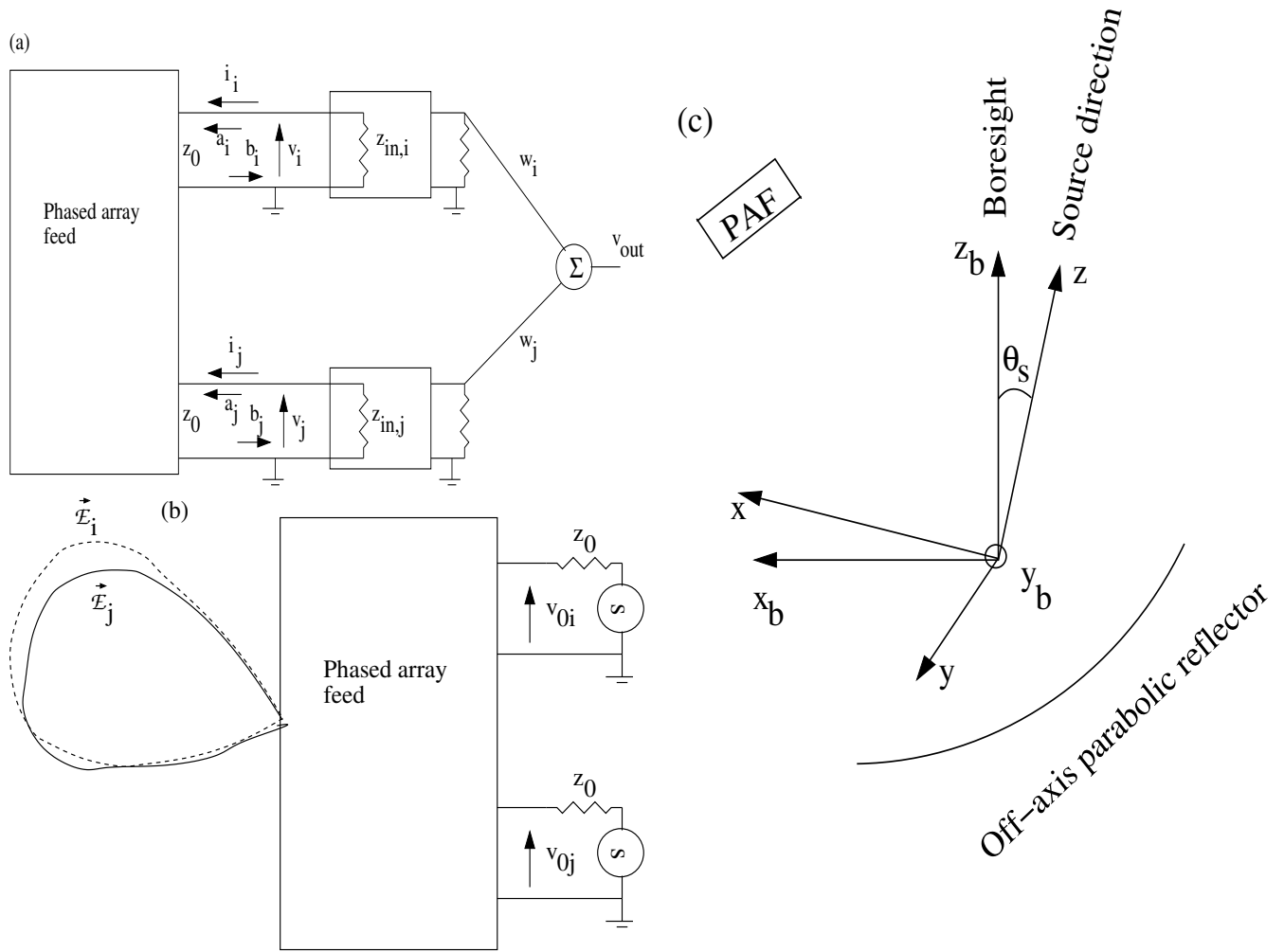


Figure 1: (a) Schematic showing the signal flow and processing in the PAF system. (b) PAF in transmitting mode. (c) PAF on an off-axis parabolic reflector. Co-ordinate system used to specify the ‘boresight’ direction and source direction are also shown (see text for details).

Theorem : Given the (spectral) impedance matrix, \mathbf{Z} , and the embedded beam patterns, $\vec{\mathcal{E}}^e$, of the PAF, given the amplifier noise parameters (R_n, g_n, ρ) and its input impedance (Z_{in}), and given the telescope geometry and source position (θ_s, ϕ_s), one can construct a characteristics matrix \mathbf{M} for the *system* (i.e. PAF + telescope + receiver). Then the best signal-to-noise ratio on the source is the maximum eigenvalue, e_{max} of \mathbf{M} .

As described below e_{max} can be converted to T_{sys}/η_{ap} from the knowledge of telescope aperture area and source flux density. The proof of the theorem is presented below.

3.1 Schematic of PAF, Impedance Matrix and Embedded beam pattern

In this section we describe the necessary background needed on the *system* to prove the theorem. A schematic of the PAF is shown in Fig. 1a. The signals from the antenna elements are brought to the ‘ports’ of the PAF through a transmission line of characteristics impedance z_0 . For simplicity we consider z_0 is equal to the reference impedance 50Ω . Let the total number of ports of the PAF be

M . The network characteristics of the PAF are specified by the impedance matrix, \mathbf{Z} , which relates the port voltages v_i and currents i_i . Another method used to specify the network characteristics is the Scattering matrix, \mathbf{S} , which relates the forward and reverse traveling waves at the port. The amplitude of these waves are a_i and b_i respectively for the forward and reverse waves. All voltages, currents and wave amplitudes are harmonic quantities (i.e. they are quantities per unit frequency interval) and their values are specified as *peak* values. For simplicity, we omit adding the term $e^{j\omega t}$. The relationship between the network parameters is discussed in Appendix A.

Fig. 1a also shows schematically the signal processing done in the PAF system. Each antenna element of the PAF is followed by a low-noise amplifier (LNA). The input impedance of the i^{th} LNA is Z_{in_i} . The signals are further amplified and scaled with a complex weight vector $\mathbf{w}^T = [w_1, w_2, \dots]$. We consider that the weights are normalized such that $\mathbf{w}^H \mathbf{w} = 1$. The scaled quantities are then added together to get the signal from a beam. The operation is also referred to as beamforming. Multiple beams are formed by adding the signals after scaling them with different weight vectors.

In addition to the network characteristics we need to specify the radiation pattern of the PAF. In Section 3.3 we show that it is convenient to express the radiation pattern in terms of the *embedded beam patterns*. The j^{th} embedded beam pattern, $\vec{\mathcal{E}}_j^e$ is defined as the beam pattern of the PAF when j^{th} port is excited with 1 V (i.e. $v_{0_j} = 1$ V) and all other ports are short circuited (i.e. $v_{0_i} = 0$ V for $i \neq j$; see Fig. 1b). The source impedance for excitation is considered to be equal to z_0 . Thus there are M embedded beam patterns, which are represented conveniently as a vector $\vec{\mathcal{E}}^e$,

$$\vec{\mathcal{E}}^e = [\vec{\mathcal{E}}_1^e, \vec{\mathcal{E}}_2^e, \dots] \quad (1)$$

These beam patterns are function of the position vector \vec{r} , the origin of the coordinate system is located at the center of the PAF (see Appendix I for further details on the coordinate system). The beam patterns are specified at the far-field i.e. $|\vec{r}| \gg \frac{2D_{array}^2}{\lambda}$, where D_{array} is the maximum physical size of the PAF and λ is the wavelength of operation of the PAF. As described below, the embedded beam patterns are scaled by the port voltage and summed up to get the resultant beam pattern of the PAF for an arbitrary set of port voltages. Hence the dimension of the embedded beam pattern is m^{-1} . At far-field, the beam pattern can be described by an outgoing spherical wave,

$$\vec{\mathcal{E}}_i^e(\vec{r}) = \vec{E}_i^e(\theta, \phi) \frac{e^{j\vec{k} \cdot \vec{r}}}{r} \quad (2)$$

where $\vec{\mathcal{E}}_i^e$ is the i^{th} embedded beam pattern, r and \hat{r} are the magnitude and the unit vector in the direction of \vec{r} respectively, $\vec{k} = \frac{2\pi}{\lambda} \hat{r}$ is the propagation vector. The vector function \vec{E}_i^e depends only on the coordinates θ, ϕ . It should be noted that the geometric phase due to the location of elements (or in other words the excitation current distribution) away from the co-ordinate center is included in \vec{E}_i^e . From the definition of embedded pattern it follows that \vec{E}_i^e is dimensionless. As in the case of network parameters, the field are harmonic quantities and for simplicity we omit the term $e^{j\omega t}$. Since the beam patterns are specified at free space the angular frequency ω and λ are related through

$$c = \frac{\omega}{2\pi} \lambda, \quad (3)$$

where c is the velocity of light in free space. Moreover the embedded magnetic field patterns are given by

$$\vec{\mathcal{H}}_i^e = \frac{\hat{k}}{z_f} \times \vec{\mathcal{E}}_i^e \quad (4)$$

where \hat{k} is the unit vector in the direction of \vec{k} and z_f is the free space impedance. The relationship between the network parameters and embedded beam patterns are discussed in Appendix A.

The radiation pattern of the PAF when excited by a set of arbitrary port voltages can be expressed in terms of the embedded beam patterns as (see Fig. 1b and also Section 3.3)

$$\begin{aligned}\vec{\mathcal{E}}(\vec{r}) &= \sum_{i=1, M} v_{0_i} \vec{\mathcal{E}}_i^e(\vec{r}) \\ &= \mathbf{V}_0^T \vec{\mathcal{E}}^e\end{aligned}\quad (5)$$

where \mathbf{V}_0 is the vector of port voltages v_{0_i} . The radiation pattern $\vec{\mathcal{E}}$ has the units V/m. At far-field, the (θ, ϕ) dependence of the radiation pattern can be written in a similar fashion,

$$\vec{E}(\theta, \phi) = \mathbf{V}_0^T \vec{E}^e. \quad (6)$$

The units of \vec{E} is V. In the report, we refer to $\vec{\mathcal{E}}^e$ and \vec{E}^e as embedded beam patterns – the \vec{r} dependence is implied in the usage of calligraphic symbol.

For our application, the PAF is placed at the prime focus of a (off-axis) parabolic antenna. A schematic showing the geometry of the configuration along with the observing source direction is shown in Fig. 1c. To specify the source direction, we consider a co-ordinate system with z_b -axis pointing toward the ‘boresight’ direction of the telescope and the $x_b - y_b$ plane coinciding with the ‘aperture plane’. The source direction is specified by the polar angle (θ_s, ϕ_s) with respect to this co-ordinate system. A second co-ordinate system with the z -axis pointing towards the source and the $x - y$ plane coinciding with the ‘projected aperture plane’ in the direction of the source is used to calculate the PAF field pattern on the projected aperture plane (see Section 3.3). The unit vectors in the direction of x, y, z axes are referred to as \hat{u}_x, \hat{u}_y and \hat{u}_z respectively.

3.2 Signal to Noise Ratio

We start the proof of the theorem by considering the signal to noise ratio (SNR) at the output of the PAF. For a typical observation with the PAF, on-source and off-source measurements are made. The SNR can then be written as

$$\text{SNR} = \frac{P_{on-source}}{P_{off-source}} \quad (7)$$

where $P_{on-source}$ is the increase in power spectral density at the output of a beam due to the source relative to the off-source spectral density, $P_{off-source}$. Below, we compute this SNR using the signal processing done in the PAF.

The output voltage per unit frequency interval after beamforming can be written as

$$v_{out} = \mathbf{w}^T \tilde{\mathbf{V}} \quad (8)$$

where $\tilde{\mathbf{V}}$ is the voltage vector at the input of the combiner (see Fig. 1a). This voltage vector can be written as a sum of at least four components;

$$\tilde{\mathbf{V}} = \tilde{\mathbf{V}}_{signal} + \tilde{\mathbf{V}}_{spill} + \tilde{\mathbf{V}}_{rec} + \tilde{\mathbf{V}}_{sky} \quad (9)$$

where $\tilde{\mathbf{V}}_{signal}, \tilde{\mathbf{V}}_{spill}, \tilde{\mathbf{V}}_{rec}$ and $\tilde{\mathbf{V}}_{sky}$ are the contributions due to source, spillover noise, receiver noise and sky background noise. For a typical application using the PAF, the output signal power

or power spectral density is measured. This power spectral density is proportional to $\langle v_{out}v_{out}^* \rangle$, which can be written as

$$\begin{aligned}\langle v_{out}v_{out}^* \rangle &= \mathbf{w}^H \langle \tilde{\mathbf{V}}\tilde{\mathbf{V}}^H \rangle \mathbf{w} \\ &= \mathbf{w}^H \tilde{\mathbf{R}} \mathbf{w} \\ &= \mathbf{w}^H \tilde{\mathbf{R}}_{signal} \mathbf{w} + \mathbf{w}^H \tilde{\mathbf{R}}_{spill} \mathbf{w} + \mathbf{w}^H \tilde{\mathbf{R}}_{rec} \mathbf{w} + \mathbf{w}^H \tilde{\mathbf{R}}_{sky} \mathbf{w}\end{aligned}\quad (10)$$

where $\tilde{\mathbf{R}}$ is the matrix of voltage correlation per unit frequency interval. Since the different voltage components are uncorrelated, $\tilde{\mathbf{R}}$ can be written as the sum of the correlations of its components, *viz.*, $\tilde{\mathbf{R}}_{signal}$, $\tilde{\mathbf{R}}_{spill}$, $\tilde{\mathbf{R}}_{rec}$ and $\tilde{\mathbf{R}}_{sky}$ which correspond to the voltage correlations due to source, spillover noise, receiver noise and sky background noise respectively. The SNR on the source is then

$$\begin{aligned}\text{SNR} &= \frac{P_{on-source}}{P_{off-source}} \\ &\approx \frac{\mathbf{w}^H \tilde{\mathbf{R}}_{signal} \mathbf{w}}{\mathbf{w}^H \tilde{\mathbf{R}}_{spill} \mathbf{w} + \mathbf{w}^H \tilde{\mathbf{R}}_{rec} \mathbf{w} + \mathbf{w}^H \tilde{\mathbf{R}}_{sky} \mathbf{w}}.\end{aligned}\quad (11)$$

The approximate sign in Eq. 11 is introduced to indicate (a) that the noise power in on-source measurement is dominated by components other than the source and (b) that the sky and spillover components are approximately same for the on-source and off-source positions. (We ignore the approximate sign below for convenience.)

We wish to write Eq. 11 in terms of open circuit voltages at the output of the PAF antenna elements. It follows from network analysis that the output voltage vector

$$\tilde{\mathbf{V}} = \mathbf{G} \mathbf{A} \mathbf{V}_{oc} \quad (12)$$

where

$$\mathbf{A} = -\mathbf{Z}_{in}(\mathbf{Z} + \mathbf{Z}_{in})^{-1}, \quad (13)$$

\mathbf{Z}_{in} is the input impedance matrix, which is a diagonal matrix with elements $Z_{in,i}$, \mathbf{G} is the overall system gain matrix, which again is a diagonal matrix and \mathbf{V}_{oc} is the open circuit voltage vector at the output of the PAF. In terms of the open circuit voltage Eq. 11 becomes

$$\begin{aligned}\text{SNR} &= \frac{\mathbf{w}_1^H \mathbf{R}_{signal} \mathbf{w}_1}{\mathbf{w}_1^H \mathbf{R}_{spill} \mathbf{w}_1 + \mathbf{w}_1^H \mathbf{R}_{rec} \mathbf{w}_1 + \mathbf{w}_1^H \mathbf{R}_{sky} \mathbf{w}_1} \\ &= \frac{\mathbf{w}_1^H \mathbf{R}_{signal} \mathbf{w}_1}{\mathbf{w}_1^H \mathbf{N} \mathbf{w}_1}\end{aligned}\quad (14)$$

where

$$\mathbf{w}_1 = \mathbf{A}^H \mathbf{G}^H \mathbf{w}, \quad (15)$$

is the modified weights and \mathbf{R}_{signal} , \mathbf{R}_{spill} , \mathbf{R}_{rec} and \mathbf{R}_{sky} are the open circuit voltage correlations corresponding to source, spillover noise, receiver noise and sky background noise respectively. We refer to \mathbf{R}_{signal} as the signal matrix, \mathbf{R}_{spill} as the spillover matrix, \mathbf{R}_{rec} as the receiver matrix and \mathbf{R}_{sky} as the sky matrix. Further, we define

$$\mathbf{N} \equiv \mathbf{R}_{spill} + \mathbf{R}_{rec} + \mathbf{R}_{sky}, \quad (16)$$

and refer to as the noise matrix. Since \mathbf{N} is a correlation matrix, it is Hermitian. Therefore it can be uniquely decomposed into products of two matrices (*i.e.* $\mathbf{N} = \mathcal{N}\mathcal{N}$) using the eigen structure of \mathbf{N} [12]. Thus Eq. 14 can be written as

$$\text{SNR} = \frac{\mathbf{w}_2^H \mathcal{N}^{-1} \mathbf{R}_{signal} \mathcal{N}^{-1} \mathbf{w}_2}{\mathbf{w}_2^H \mathbf{w}_2} \quad (17)$$

where

$$\mathbf{w}_2 = \mathcal{N}\mathbf{w}_1. \quad (18)$$

We define the system characteristics matrix as

$$\mathbf{M} \equiv \mathcal{N}^{-1}\mathbf{R}_{signal}\mathcal{N}^{-1}. \quad (19)$$

From Eq. 17 the maximum SNR is given by the maximum eigenvalue, e_{max} , of \mathbf{M} . Using Eq. 15 and 18, the weight vector \mathbf{w}_{max} that needs to be applied at the output to get the maximum SNR is

$$\mathbf{w}_{max} = (\mathbf{G}^H)^{-1} (\mathbf{A}^H)^{-1} \mathcal{N}^{-1} \mathbf{w}_{2max} \quad (20)$$

where \mathbf{w}_{2max} is the eigenvector corresponding to e_{max} .

We now convert e_{max} to the ratio $\frac{T_{sys}}{\eta}$. The power spectral density due to the source is proportional to the antenna temperature T_A , which can be written as

$$T_A = \frac{1}{2} \frac{S_{source}}{k_B} A_{ap} \eta_{ap} \quad (21)$$

where S_{source} is the flux density of the source used for the measurement, A_{ap} is the aperture area of the antenna, k_B is the Boltzmann constant and $\eta_{ap} = \eta_{tap}\eta_{spill}$ is the aperture efficiency of the system. η_{tap} and η_{spill} are the taper and spillover efficiencies respectively. The off-source power spectral density is proportional to the system temperature T_{sys} . Then the SNR can be written as

$$\text{SNR} = \frac{T_A}{T_{sys}}. \quad (22)$$

Using Eq. 17 and 22, the best performance of PAF is

$$\frac{T_{sys}}{\eta_{ap}} = \frac{S_{source} A_{ap}}{2k_B e_{max}}. \quad (23)$$

The computation of the signal, receiver, spillover, and sky correlation matrices in order to construct \mathbf{M} is discussed below. We first develop the method used to compute the open circuit voltage at the output of the array due to incident radiation, which is presented in Section 3.3.

3.3 PAF in Receiving mode

To compute the open circuit voltage at the output of the PAF in receiving mode, we start with the Lorentz reciprocity theorem. This theorem is derived from Maxwell's equation with no further assumptions made. The particular form of the theorem we use is

$$\oint_A \vec{\mathcal{L}} \cdot \hat{n} \, dA = 0 \quad (24)$$

where

$$\vec{\mathcal{L}} \equiv \vec{\mathcal{E}} \times \vec{\mathcal{H}}_r - \vec{\mathcal{E}}_r \times \vec{\mathcal{H}}. \quad (25)$$

The fields $\vec{\mathcal{E}}, \vec{\mathcal{H}}, \vec{\mathcal{E}}_r$ and $\vec{\mathcal{H}}_r$ are two solutions to Maxwell's equation within a source free volume and on the enclosed surface A , \hat{n} is the unit vector inward to the surface normal to the elementary area dA [13]. We consider $\vec{\mathcal{E}}, \vec{\mathcal{H}}$ as the electric and magnetic fields, respectively, when the PAF is in transmitting mode, $\vec{\mathcal{E}}_r, \vec{\mathcal{H}}_r$ as the electric and magnetic fields, respectively, incident on the PAF when the array is in receiving mode. By appropriately choosing the surface, the integration can be

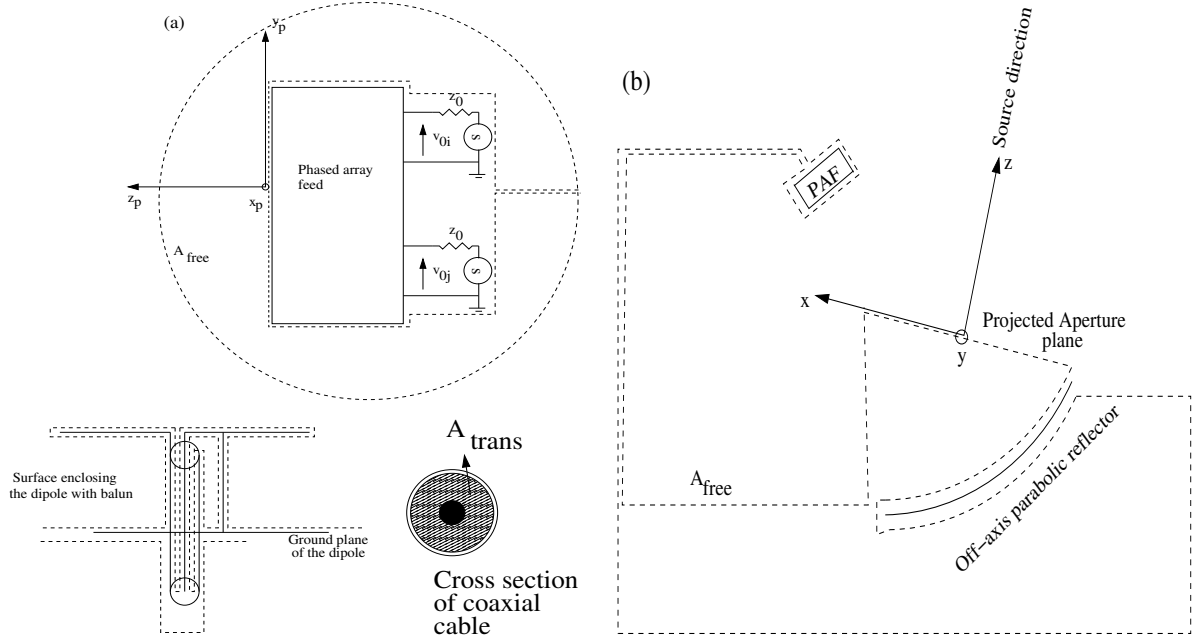


Figure 2: (a) Schematic showing the enclosed source free volume for the application of Lorentz theorem (see Section 3.3). Details of the source free surface enclosing the dipole and balun and inside the transmission line is also shown. (b) PAF on an off-axis parabolic reflector and the corresponding enclosed source free volume used to get the open circuit voltage due to a source.

broken up into two parts – (a) integration over the surface area, A_{trans} inside the transmission line and (b) the integration over the surface, A_{free} outside the PAF (see Fig. 2). The integral in all other parts of the surface close to the metal surface is zero since the tangential component of the electric field vanishes. We consider the ports of the PAF are connected to the signal sources with source impedance z_0 during transmission, and during reception, all ports are terminated with the impedance z_0 . As shown in Fig. 2, the x_p, y_p, z_p coordinate system is located on the PAF. The axis z_p and the unit vectors \hat{u}_z^p along its direction are parallel to the transmission line. The field in the wave guide for the transmission and reception cases can be written as

$$\vec{\mathcal{E}} = \sqrt{z_0}(a_i + b_i)\vec{e}(x_p, y_p)e^{-j\beta z_p} \quad (26)$$

$$\vec{\mathcal{H}} = \frac{1}{z_0}\hat{u}_z^p \times \vec{\mathcal{E}} \quad (27)$$

$$\vec{\mathcal{E}}_r = \sqrt{z_0}b_{r_i}\vec{e}(x_p, y_p)e^{j\beta z_p} \quad (28)$$

$$\vec{\mathcal{H}}_r = -\frac{1}{z_0}\hat{u}_z^p \times \vec{\mathcal{E}}_r \quad (29)$$

where a_i, b_i are the traveling wave amplitudes in the transmission case, b_{r_i} is the traveling wave amplitude in the receiving case, $\vec{e}(x_p, y_p)$ is the normalized electric field inside the transmission line and β is the propagation constant in the transmission line. $\vec{e}(x_p, y_p)$ is a function of the geometric parameters of the transmission line [14]. The integral over A_{trans} can then be written as

$$\int_{A_{trans}} \vec{\mathcal{L}} \cdot \hat{n} dA = -2 \sum_{i=1, M} b_{r_i}(a_i + b_i) \int_{A_{trans}} |\vec{e}(x_p, y_p)|^2 dA \quad (30)$$

The transmitted power in *each* transmission line or port can be written as

$$\operatorname{Re} \frac{1}{2} \int_{A_{trans}} \vec{\mathcal{E}} \times \vec{\mathcal{H}}^* \cdot \hat{n} \, dA = \frac{1}{2} |a_i|^2 + \frac{1}{2} |b_i|^2 \quad (31)$$

Using Eq. 26 and 27, Eq. 31 can be written as

$$(a_i + b_i)(a_i + b_i)^* \int_{A_{trans}} |\vec{e}(x_p, y_p)|^2 dA = |a_i|^2 + |b_i|^2. \quad (32)$$

Substituting Eq. 32 in Eq. 30, the integration over A_{trans} becomes

$$\begin{aligned} \int_{A_{trans}} \vec{\mathcal{L}} \cdot \hat{n} \, dA &= -2 \sum_{i=1, M} b_{r_i} (a_i - b_i) \\ &= - \sum_{i=1, M} v_{oc_i} i_{0_i} \\ &= -\mathbf{V}_{oc}^T \mathbf{I}_0 \end{aligned} \quad (33)$$

where \mathbf{V}_{oc} is the open circuit (peak) voltage vector with elements v_{oc_i} , induced by the receiving field and \mathbf{I}_0 is the excitation (peak) current vector with elements i_{0_i} , which produces the transmission beam pattern (see Appendix A for the relationship between traveling wave amplitude and voltages and currents). Substituting Eq. 33 in Eq. 24 we get

$$\begin{aligned} \mathbf{V}_{oc}^T \mathbf{I}_0 &= \int_{A_{free}} \vec{\mathcal{L}} \cdot \hat{n} \, dA \\ &= \int_{A_{free}} \left(\vec{\mathcal{E}} \times \vec{\mathcal{H}}_r - \vec{\mathcal{E}}_r \times \vec{\mathcal{H}} \right) \cdot \hat{n} \, dA \end{aligned} \quad (34)$$

The right hand side of Eq. 34 can be written as a summation analogues to the left hand side, i.e.

$$\begin{aligned} \vec{\mathcal{E}} &= \sum_{i=1, M} v_{0_i} \vec{\mathcal{E}}_i^e \\ &= \mathbf{V}_0^T \vec{\mathcal{E}}^e \end{aligned} \quad (35)$$

where the elements of the vector $\vec{\mathcal{E}}^e$ are $\vec{\mathcal{E}}_i^e$, which are the radiation patterns of the PAF for $v_{0_i} = 1V$ for $i = j$ and 0 V for $i \neq j$. We define the elements of the vector $\vec{\mathcal{E}}^e$ as the *embedded beam patterns*. Using Eq. 35 we can write Eq. 34 as

$$\mathbf{V}_{oc}^T \mathbf{I}_0 = \mathbf{V}_0^T \int_{A_{free}} \left(\vec{\mathcal{E}}^{eT} \times \mathcal{I} \vec{\mathcal{H}}_r - \mathcal{I} \vec{\mathcal{E}}_r \times \vec{\mathcal{H}}^e \right) \cdot \hat{n} \, dA, \quad (36)$$

where \mathcal{I} is the identity matrix, $\vec{\mathcal{H}}^e$ is the embedded magnetic field patterns (see Appendix J for an explanation of the notation used in Eq. 36). Since Eq. 36 is true for arbitrary excitation voltages it follows that

$$\mathbf{V}_{oc} = \mathbf{Z} \int_{A_{free}} \left(\vec{\mathcal{E}}^{eT} \times \mathcal{I} \vec{\mathcal{H}}_r - \mathcal{I} \vec{\mathcal{E}}_r \times \vec{\mathcal{H}}^e \right) \cdot \hat{n} \, dA, \quad (37)$$

where we have made use of the relation $\mathbf{V}_0 = \mathbf{Z} \mathbf{I}_0$ between the excitation voltage and current (see Appendix A). We show in Appendix C that Eq. 37 gives the voltage correlation expected from the first and second law of thermodynamics when the PAF is in thermal equilibrium with a black body field. Below we evaluate the right hand side of Eq. 37 for two cases of interest here, *viz* (a) incident plane wave radiation field and (b) incident radiation from a (compact) source when the PAF is on the telescope.

3.3.1 Plane Wave

Let the PAF be incident by a plane wave of field $\vec{E}_{inc} = E_{inc}\hat{p}$, where \hat{p} denotes a vector parallel to the polarization of the electric field. The incident direction \vec{r} is parallel to the propagation vector \vec{k}_{inc} . The surface considered for the integration is shown in Fig. 2a. Using stationary-phase algorithm, the integral over A_{free} can be written as [13]

$$\int_{A_{free}} \vec{\mathcal{L}} \cdot \hat{n} \, dA = \frac{jk\lambda^2 r e^{jkr}}{\pi z_f} E_{inc} \hat{p} \cdot \vec{\mathcal{E}} \quad (38)$$

where $\vec{\mathcal{E}}$ is the beam pattern of the PAF for an arbitrary excitation, $r = |\vec{r}|$, $k = |\vec{k}_{inc}|$, z_f is the free space impedance. This equation is valid for excitation that produces the embedded beam pattern as well. Thus by writing Eq. 38 in terms of the embedded beam pattern and substituting in Eq. 37 we get (see Appendix J for an explanation of notation used in Eq. 39)

$$\mathbf{V}_{oc} = \frac{j4\pi r e^{jkr}}{k z_f} E_{inc} \mathbf{Z} \mathbf{I} \hat{p} \cdot \vec{\mathcal{E}}^e. \quad (39)$$

3.3.2 PAF on the telescope

We now consider the case when the PAF is placed at the prime focus of a telescope with a parabolic reflector. An appropriate closed surface enclosing a source free region for the integration is shown in Fig. 2b for a (off-axis) parabolic antenna (eg. Green Bank Telescope; GBT). The source is located at an angle (θ_s, ϕ_s) from the boresight of the telescope. The major contribution to the integral over the surface A_{free} comes from the projected aperture plane (see Fig. 2b). Although the surface geometry of A_{free} has changed compared to Fig. 2a, the part (a) of the surface integral discussed in Section 3.3 remain the same. The part of the surface close to the reflector will not contribute to the integral because the tangential component of the field should be zero on the surface of the metal. The phase difference between the incoming waves and the embedded beam patterns changes rapidly in all other parts of the surface A_{free} so that the net contribution to the integral will be zero. Thus

$$\int_{A_{free}} \vec{\mathcal{L}} \cdot \hat{n} \, dA = \int_{A_{pap}} \vec{\mathcal{L}} \cdot \hat{n} \, dA \quad (40)$$

where A_{pap} denotes integration over the projected aperture plane. Using Eq. 37, the open circuit voltage due to the source is

$$\mathbf{V}_{oc} = \mathbf{Z} \int_{A_{pap}} \left(\vec{\mathcal{E}}_{pap}^e \cdot \mathbf{I} \vec{\mathcal{H}}_r - \mathbf{I} \vec{\mathcal{E}}_r \cdot \vec{\mathcal{H}}_{pap}^e \right) \cdot \hat{n} \, dA. \quad (41)$$

Here $\vec{\mathcal{H}}_r$ and $\vec{\mathcal{E}}_r$ are fields on the projected aperture plane due to the source, $\vec{\mathcal{E}}_{pap}^e$ and $\vec{\mathcal{H}}_{pap}^e$ are embedded beam patterns propagated to the projected aperture plane after reflection from the parabolic surface. By representing the incident field due to the source on the projected aperture plane as $\vec{E}_{inc} = E_{inc}\hat{p}$ and the embedded magnetic field as $\vec{\mathcal{H}}_{pap}^e = -\frac{1}{z_f} \mathbf{I} \hat{n} \times \vec{\mathcal{E}}_{pap}^e$, Eq. 41 becomes

$$\mathbf{V}_{oc} = 2 \frac{\mathbf{Z}}{z_f} \int_{A_{pap}} E_{inc} \mathbf{I} \hat{p} \cdot \vec{\mathcal{E}}_{pap}^e \, dA. \quad (42)$$

Note that E_{inc} and \hat{p} are in general functions of positions in the projected aperture plane.

For the case of an astronomical source the incident field can be broken up into two orthogonal polarizations, the directions are conveniently taken along the x and y axis, i.e.,

$$\vec{E}_{inc} = E_{inc,x}\hat{u}_x + E_{inc,y}\hat{u}_y. \quad (43)$$

Here $E_{inc,x}$ and $E_{inc,y}$ are random variables and for simplicity we assume that they are uncorrelated, i.e., the source is unpolarized. Eq. 42 can then be written as

$$V_{oc} = 2\frac{Z}{z_f} \int_{A_{pap}} \left(\mathcal{I}E_{inc,x}\mathcal{E}_{pap,x}^e + \mathcal{I}E_{inc,y}\mathcal{E}_{pap,y}^e \right) dA \quad (44)$$

where $\mathcal{E}_{pap,x}^e$ and $\mathcal{E}_{pap,y}^e$ are vectors of the x and y components of the embedded beam patterns, \mathcal{E}_{pap}^e , respectively. We show in Appendix E that this equation gives the well known relationship between source antenna temperature and aperture efficiency.

3.4 The Spillover matrix

The PAF placed at the prime focus of the telescope picks up thermal radiation from the ground. These radiation are received by the PAF from the solid angles larger than the solid angle subtended by the parabolic reflector. We refer to the total solid angle from which the ground radiation is picked up as Ω_{spill} . We consider the ground radiation field as a set of plane waves incident at different directions. The open circuit voltage due to a plane wave in a direction \vec{r} is given by Eq. 39. The correlation of this voltage is

$$\begin{aligned} \mathbf{R}_1 &= \langle \mathbf{V}_{oc1}\mathbf{V}_{oc1}^H \rangle \\ &= \frac{(4\pi)^2 r^2}{k^2 z_f^2} \left\langle \left(E_{inc} \mathbf{Z} \mathcal{I} \hat{p} \cdot \vec{\mathcal{E}}^e \right) \left(\vec{\mathcal{E}}^{eH} \cdot \mathcal{I} \hat{p} \mathbf{Z}^H E_{inc}^* \right) \right\rangle \end{aligned} \quad (45)$$

where \mathbf{R}_1 is the correlation of open circuit voltage \mathbf{V}_{oc1} due to a plane wave. For thermal radiation, E_{inc} is a stationary random variable and \hat{p} has random orientation. Therefore, without loss of generality, $E_{inc}\hat{p}$ can be decomposed into two orthogonal directions of the field $\vec{\mathcal{E}}_i^e$. The two polarization components of $E_{inc}\hat{p}$ are uncorrelated for the thermal radiation field. Keeping in mind that a port of PAF is sensitive to one of the polarizations, Eq. 45 can be written as

$$\mathbf{R}_1 = \frac{(4\pi)^2 r^2}{k^2 z_f^2} \frac{\langle E_{inc} E_{inc}^* \rangle}{2} \mathbf{Z} \vec{\mathcal{E}}^e \cdot \vec{\mathcal{E}}^{eH} \mathbf{Z}^H. \quad (46)$$

In the Rayleigh-Jeans approximation the thermal field is related to the brightness temperature

$$\frac{1}{z_f} \langle E_{inc} E_{inc}^* \rangle = \frac{2k_B T_g}{\lambda^2} d\Omega, \quad (47)$$

where T_g is the physical temperature of the ground. Using Eq. 47, \mathbf{R}_1 can be written as

$$\mathbf{R}_1 = \frac{4k_B T_g r^2}{z_f} \mathbf{Z} \vec{\mathcal{E}}^e \cdot \vec{\mathcal{E}}^{eH} \mathbf{Z}^H d\Omega. \quad (48)$$

Since the spillover noise is due to thermal radiation from the ground, the voltages due to plane waves from different directions are uncorrelated. The resultant voltage correlation due to spillover

noise is then

$$\begin{aligned}
\mathbf{R}_{spill} &= \int_{\Omega_{spill}} \mathbf{R}_1 d\Omega, \\
&= \frac{4k_B T_g}{z_f} \mathbf{Z} \left(\int_{\Omega_{spill}} \vec{\mathcal{E}}^e \cdot \vec{\mathcal{E}}^{eH} r^2 d\Omega \right) \mathbf{Z}^H, \\
&= \frac{4k_B T_g}{z_f} \mathbf{Z} \left(\int_{\Omega_{spill}} \vec{\mathbf{E}}^e \cdot \vec{\mathbf{E}}^{eH} d\Omega \right) \mathbf{Z}^H, \tag{49}
\end{aligned}$$

$$= \frac{4k_B T_g}{z_f} \mathbf{Z} \mathbf{C}_{ce1} \mathbf{Z}^H. \tag{50}$$

where Ω_{spill} is the solid angle over which the PAF embedded beam patterns are receiving radiation from ground. We also made use of Eq. 2 to introduce the embedded beam patterns $\vec{\mathbf{E}}^e$ in Eq. 49. We define

$$\mathbf{C}_{ce1} \equiv \int_{\Omega_{spill}} \vec{\mathbf{E}}^e \cdot \vec{\mathbf{E}}^{eH} d\Omega, \tag{51}$$

which is the correlation matrix of the embedded beam patterns integrated over Ω_{spill} . In Appendix D we use Eq. 50 to expressed the spillover noise in terms of a physical temperature, referred to as spillover temperature. We also show that the derived spillover temperature gives the well known relationship between the ground temperature and the spillover efficiency when applied to a single port antenna.

3.5 The Signal Matrix

The open circuit voltage at the ports of the PAF when observing an astronomical source is given by Eq. 44. The correlation of the voltage due to source, \mathbf{V}_{oc_s} can be written as

$$\begin{aligned}
\mathbf{R}_{signal} &= \langle \mathbf{V}_{oc_s} \mathbf{V}_{oc_s}^H \rangle \\
&= \frac{4}{z_f^2} \mathbf{Z} \left\langle \left(\int_{A_{pap}} \mathcal{I} E_{inc,x} \mathcal{E}_{pap,x}^e + \mathcal{I} E_{inc,y} \mathcal{E}_{pap,y}^e dA \right) \right. \\
&\quad \left. \left(\int_{A_{pap}} \mathcal{E}_{pap,x}^{eH} \mathcal{I} E_{inc,x}^* + \mathcal{E}_{pap,y}^{eH} \mathcal{I} E_{inc,y}^* dA \right) \right\rangle \mathbf{Z}^H \tag{52}
\end{aligned}$$

$$\begin{aligned}
&= \frac{4}{z_f} \frac{S_{source}}{2} \mathbf{Z} \left(\int_{A_{pap}} \vec{\mathcal{E}}_{pap}^e dA \right) \cdot \left(\int_{A_{pap}} \vec{\mathcal{E}}_{pap}^e dA \right)^H \mathbf{Z}^H \\
&= \frac{2S_{source}}{z_f} \mathbf{Z} \mathbf{C}_{Ie} \mathbf{Z}^H. \tag{53}
\end{aligned}$$

where we define

$$\mathbf{C}_{Ie} \equiv \left(\int_{A_{pap}} \vec{\mathcal{E}}_{pap}^e dA \right) \cdot \left(\int_{A_{pap}} \vec{\mathcal{E}}_{pap}^e dA \right)^H \tag{54}$$

which is the correlation matrix of the *net* aperture fields due to embedded beam patterns. To arrive at Eq. 53, we used the relationship $\frac{1}{z_f} \langle E_{inc,x} E_{inc,x}^* \rangle = \frac{1}{z_f} \langle E_{inc,y} E_{inc,y}^* \rangle = \frac{S_{source}}{2}$ and, for simplicity, $\langle E_{inc,x} E_{inc,y}^* \rangle = \langle E_{inc,y} E_{inc,x}^* \rangle = 0$ for an unpolarized source of flux density S_{source} . Note that \mathbf{C}_{Ie} is a function of source position θ_s, ϕ_s . In Appendix E we use Eq. 53 to derive an expression for the

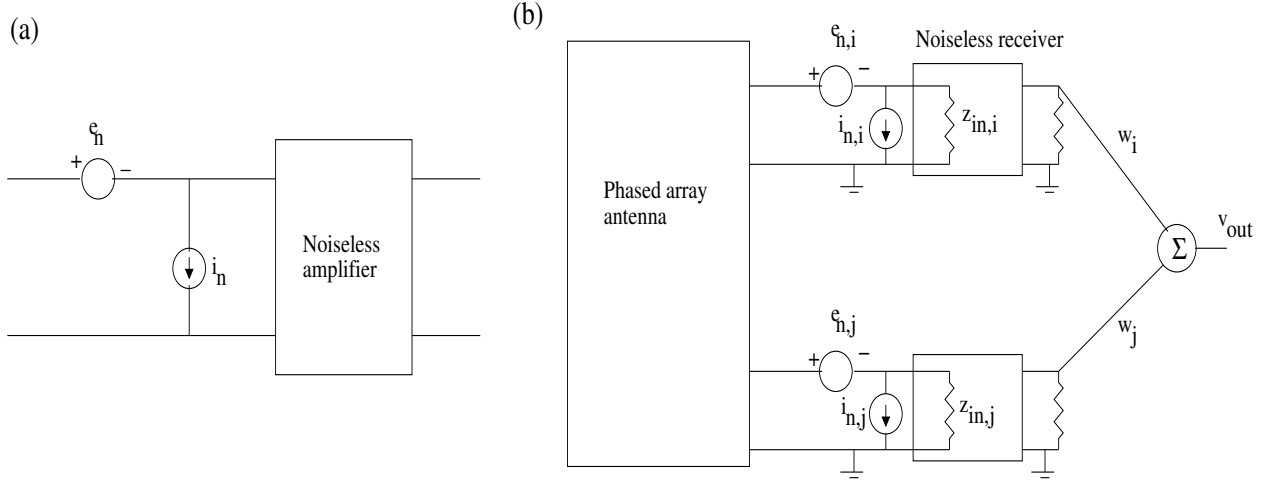


Figure 3: (a) Schematic showing the noise voltage and current generators to model the noise properties of a low-noise amplifier (LNA). (b) The network model of the PAF system along with the noise voltage and current generators of the LNA. $z_{in,i}$, $z_{in,j}$ etc are the input impedance of the amplifier

source antenna temperature. We also show that the expression for antenna temperature reduces to the well known relationship between source flux density, physical area of the telescope aperture, and aperture efficiency for a single port antenna.

3.6 The Receiver Matrix

To derive the receiver matrix, we need the noise parameters, R_n , g_n and ρ (defined below), of the amplifier in addition to the impedance matrix of the PAF. It is well known that the spectral (or spot) noise factor of noisy two-ports is equivalent to noise-free two-ports plus two (in general) partially correlated noise generators[15]. A convenient representation is to place a noise voltage generator (e_n) in series and a noise current generator (i_n) in parallel to the noise-free two-ports (see Fig 3a). The noise voltage and current fluctuations per unit frequency interval, $\langle e_n^2 \rangle$ and $\langle i_n^2 \rangle$ respectively, and their complex correlation coefficient per unit frequency interval ρ are expressed in terms of the noise parameters as

$$\langle e_n^2 \rangle = 4k_B T_0 R_n \quad (55)$$

$$\langle i_n^2 \rangle = 4k_B T_0 g_n \quad (56)$$

$$\rho = \frac{\langle e_n^* i_n \rangle}{\sqrt{\langle e_n^2 \rangle \langle i_n^2 \rangle}} \quad (57)$$

where k_B is the Boltzmann constant, $T_0 = 290$ K, R_n is the noise resistance and g_n is the noise conductance.

Fig. 4b shows the network model of PAF along with the noise generators of the LNA. For simplicity, we assume the noise contribution from the receiver stages following the LNA can be neglected. From network analysis, the open circuit voltage vector, \mathbf{V}_{oc_r} , due to LNA noise is

$$\mathbf{V}_{oc_r} = \mathbf{E}_n + \mathbf{Z} \mathbf{I}_n, \quad (58)$$

where \mathbf{E}_n is a diagonal matrix with elements $e_{n,i}$, the noise voltage generators of the LNA, \mathbf{I}_n is a diagonal matrix with elements $i_{n,i}$, the noise current generators of the LNA and \mathbf{Z} is the impedance

matrix of the PAF. The open circuit voltage correlation is then

$$\begin{aligned}\mathbf{R}_{rec} &= \langle \mathbf{V}_{oc_r} \mathbf{V}_{oc_r}^H \rangle \\ &= \langle \mathbf{E}_n \mathbf{E}_n^H \rangle + \mathbf{Z} \langle \mathbf{I}_n \mathbf{E}_n^H \rangle + \\ &\quad \langle \mathbf{E}_n \mathbf{I}_n^H \rangle \mathbf{Z}^H + \mathbf{Z} \langle \mathbf{I}_n \mathbf{I}_n^H \rangle \mathbf{Z}^H.\end{aligned}\quad (59)$$

Here $\langle \mathbf{E}_n \mathbf{E}_n^H \rangle$, $\langle \mathbf{I}_n \mathbf{I}_n^H \rangle$ and $\langle \mathbf{I}_n \mathbf{E}_n^H \rangle$ are diagonal matrices of noise fluctuations and their correlations. For identical LNAs connected to the PAF, using Eq. 55 to 57, we get

$$\mathbf{R}_{rec} = 4k_B T_0 \left(R_n \mathcal{I} + \sqrt{R_n g_n} (\rho \mathbf{Z} + \rho^* \mathbf{Z}^H) + g_n \mathbf{Z} \mathbf{Z}^H \right). \quad (60)$$

In Appendix F, we use Eq. 60 to get the receiver temperature for the PAF. We also show that the receiver temperature of PAF can be written as a generalization of the equation used to express the receiver temperature of a single antenna followed by an LNA.

3.7 The Sky Matrix

The sky background radiation has components due to Cosmic microwave background (CMB), galactic and extragalactic radiation. The open circuit voltage correlation due to these components adds up since the voltages due to the different components are uncorrelated. The correlation due to CMB can be derived by considering the PAF + telescope in a black-body radiation field with temperature $T_{cmb} = 2.7$ K. The voltage correlation \mathbf{R}_{cmb} in this case is (see Appendix B)

$$\mathbf{R}_{cmb} = 2k_B T_{cmb} (\mathbf{Z} + \mathbf{Z}^H). \quad (61)$$

The voltage correlation due to other sky background components can be calculated from a knowledge of their visibility function. In this report, we take

$$\mathbf{R}_{sky} \approx 2k_B T_{sky} (\mathbf{Z} + \mathbf{Z}^H) \quad (62)$$

where

$$T_{sky} = T_{cmb} + T_{bg, \nu_0} \left(\frac{\nu}{\nu_0} \right)^{-2.7} \quad (63)$$

is the temperature of the sky background at the observed off-source position. Here T_{bg, ν_0} is the galactic background radiation temperature at ν_0 and ν is the frequency at which \mathbf{R}_{sky} is computed.

4 PAF model

As described in Section 3, we need (1) the impedance matrix of PAF, (2) the embedded beam pattern of the PAF, (3) the amplifier noise parameters, (4) the telescope geometry and (5) the ground and sky background temperature for modeling. The impedance matrix and embedded beam patterns are obtained from simulation using a commercial software package (CST). CST package is a “software for the simulation of electromagnetic fields in arbitrary three-dimensional structures” (see https://en.wikipedia.org/wiki/Computer_Simulation_Technology). The mutual coupling effects between elements in the array are included in the CST simulation. To describe the steps involved in the modeling process we consider a 19 dual polarized dipole PAF, shown in Fig. 4. The dipoles are referred to as kite dipoles (see Fig. 4). The dipoles are kept in front of a ground plane. The transmission lines at the end of the dipoles are 50 Ω co-axial cable. The mechanical dimensions of the PAF are shown in Fig. 4.

4.1 CST simulation

A mechanical model of the PAF is created in CST first (see Fig. 5). The model is created by importing the Autodesk Inventor (see https://en.wikipedia.org/wiki/Autodesk_Inventor) CAD model of a dipole pair. We wrote a Visual Basic program in CST to place copies of the dipole at the 19 locations. The ground plane is created in CST. The ground plane and dipoles are assigned with Perfect-electric-conductor (PEC) in CST. The dielectric material in the coaxial cable are assigned with (loss-less) teflon material. Waveguide ports are connected to the 19×2 coaxial input of the PAF for excitation. A hexahedral mesh size of $\lambda/20$ is used for running the Transient solver. Other details on meshing are given in Fig. 6. The solution accuracy in the solver is set to -40 dB and the frequency range is set to 1 – 2 GHz. The solver takes about 200 hrs to provide the results. The results of interest for the PAF modeling are (a) Scattering matrix as a function of frequency and (b) the beam patterns as a function of frequency. The CST computes the beam patterns when one port is excited with a 50Ω source and all other ports are terminated with 50Ω . This computation is repeated for all the 19×2 ports. We export the Scattering matrix in TOUCHSTONE format which are normalized to 50Ω reference impedance. The beam patterns are exported in ‘source format’ and are sampled at 5° interval in θ, ϕ . The coordinate system (x-y-z) used to obtain the beam patterns is shown in Fig. 5. The origin of this coordinate system is located at the intersection of the ground plane with dipole 1. Some basic sanity checks on the CST products are done using MATLAB programs as described in Appendix G before further proceeding with the modeling.

4.2 MATLAB simulation

The MATLAB simulation starts with the computation of (a) the impedance matrix from the Scattering matrix as described in Appendix A, and (b) the embedded beam patterns as described in Appendix H. The embedded beam patterns are used to compute the beam correlation matrices C_{Ce1} (Eq. 51) and C_{Ie} (Eq. 54). These are functions of position angle of the source as well as the geometry of the telescope. The correlation matrices are computed for 10 offset angles away from boresight. The telescope geometry used is that of GBT. The embedded beam patterns are propagated to the projected aperture plane using Geometric optics approximation for each offset angle. To compute \mathbf{R}_{rec} (Eq. 60), we need the amplifier noise parameters. These parameters are taken from S. Weinreb’s design [16]. The values used for the noise parameters are $R_n = 0.7 \Omega$, $g_n = 1.3 \times 10^{-4} \Omega^{-1}$, $\rho = 0.1622 + j0.2040$, $Z_{opt} = 72 + j15 \Omega$ and that for the input impedance is 50Ω . The noise parameters are measured at 1.6 GHz and assumed to be constant over 1 to 2 GHz. The values used for other quantities needed to construct the system characteristics matrix are $T_g = 300 \text{ K}$, $T_{cmb} = 2.7 \text{ K}$, $T_{bg, \nu_0} = 0.7 \text{ K}$, $\nu_0 = 1.42 \text{ GHz}$ and a model for Virgo A flux density. The background temperature is the temperature at the observed off-source position obtained from [17]. The spectral index of sky background temperature is taken as -2.7 . The model used for Virgo A flux density is 285 Jy at 1 GHz with a spectral index of -0.856 . The characteristics matrix \mathbf{M} is then constructed using Eq. 19. The maximum eigenvalue of \mathbf{M} is determined, which is used to get the best $\frac{T_{sys}}{\eta_{ap}}$ (Eq. 23). The weight vector corresponding to the best $\frac{T_{sys}}{\eta_{ap}}$ are obtained using Eq. 20. The gain matrix is taken as identity matrix to get the weights. The modeling program provides $\frac{T_{sys}}{\eta_{ap}}$ and weight vector as a function of frequency and offset positions ($\theta_s, \phi_s = 0$) from boresight.

4.3 Excess noise temperature

The model presented here is for loss-less PAF and thus will not take into account of antenna loss. Any increase in receiver temperature due to change in amplifier noise parameters compared to

Table 1: Excess noise contribution to the receiver temperature

Noise contribution included in the model	
Loss in thermal transition	4 K
Excess noise due to replacement transistor	5 K
Unaccounted excess noise	5 K
Possible origin of unaccounted noise	
Antenna Loss	? K
Excess noise in the down converter ¹	~ 4 K
Excess spillover noise due to scattering from feed support	? K

¹ https://safe.nrao.edu/wiki/pub/Main/PafDevelop/Test_of_PAF_Backend_Amplitude_and_Noise_Linearity.docx

the value used in the model (for example replaced amplifiers) and transmission line loss ahead of amplifier is not accounted in the model. Some of these noise contributions are measured in the laboratory. When comparing the model results with measurements, the open circuit voltage correlation due to these noise contributions are assumed to be of the form given in Eq. 61 with T_{cmb} replaced by the measured (frequency independent) excess noise temperature. This noise correlation is added to the noise matrix, defined in Eq. 16, while obtaining $\frac{T_{sys}}{\eta_{ap}}$ from the model.

5 Comparison with measurement

A set of measurements using the Kite array on the GBT was made in January 2015. The details of the measurements are given in Roshi et al. (2015)[1]. Comparison of results from a previous version of the model with these measurements are also presented in [1]. The two major improvements in the model presented here are : (1) improvement in the computation of embedded beam pattern and (2) the orientation of the Kite array on the GBT is correctly accounted for as described in Appendix I. With these improvements, the unaccounted noise temperature needed to match the measured $\frac{T_{sys}}{\eta_{ap}}$ toward Virgo A with the model is 5 K compared to 8 K noted in [1]. Also the aperture efficiency predicted by the best fit model is 65% compared to 70% noted in [1]. Below we provide a detail comparison of January 2015 measurements and model results.

5.1 Boresight beam $\frac{T_{sys}}{\eta_{ap}}$ measured on Virgo A

We compared $\frac{T_{sys}}{\eta_{ap}}$ vs frequency obtained from Virgo A measurements made on 25 January 2015 (TG14B_913_02, scans 25 to 48; see Roshi et al. (2015)[1]) with the model predictions. In Fig. 7, we show model $\frac{T_{sys}}{\eta_{ap}}$ for 4 receiver temperatures along with measured values. The 4 receiver temperatures at 1.5 GHz are (1) those with amplifier noise alone which is ~ 8 K, (2) with addition of losses in the thermal transition which gives ~ 12 K, (3) with the excess noise due to replacement transistor which gives ~ 17 K and (4) with an excess noise of 5 K which give ~ 22 K. Table 1 summarizes the additional contributions to the receiver temperature over that due to the amplifier noise alone (see also Roshi et al. 2015[1]). A 5 K excess noise of unknown origin need to be added to the receiver temperature (i.e. ~ 22 K) to match model prediction with the measured value (see Fig 7). In Table 1, we list possible origin for this excess noise temperature.

Fig 8 shows the model aperture efficiency, spillover efficiency, receiver temperature and system

temperature vs frequency. The aperture and spillover efficiencies between 1.3 and 1.7 GHz are about 65 % and 98 % respectively.

5.2 Off-boresight beam $\frac{T_{sys}}{\eta_{ap}}$ at 1.7 GHz

The off-boresight beam $\frac{T_{sys}}{\eta_{ap}}$ measurements were obtained from ‘grid’ observations toward Virgo A at 1.7 GHz (observation made on 25 January 2015 TGBT14B_913_02, scans 49 to 489; see Roshi et al. (2015)[1]). Fig. 9 shows the model $\frac{T_{sys}}{\eta_{ap}}$ at 1.7 GHz vs offset angle along with the measurements. The model values are obtained for receiver temperature ~ 22 K at 1.5 GHz (see Section 5.1). As seen in Fig. 9, the predicted values match the measured values very well for frequency 1.7 GHz.

Fig 10 shows the model aperture efficiency, spillover efficiency, receiver temperature and system temperature vs offset angle from boresight direction. The aperture efficiency drops significantly below 65 % beyond 6’ offset angle, which, as shown in Roshi et al. (2015)[1], is due to the finite size of the PAF.

5.3 Comparison of measured noise and signal correlations with the model

We compare the noise correlation coefficient measured at an off-source position with model values. Fig 11 shows the noise correlation of dipole 1 with rest of the dipoles for a set of frequencies. The modeled and measured values matched reasonably well. Fig 12 shows the noise correlation as a function of the relative separation of the dipole in the array. These plots show all the correlation coefficients between dipole pairs. There are some general agreements between modeled and measured values.

We also compare the correlation due to signal from source between model and measurement. Fig. 13 plots the correlation of dipole 1 with rest of the dipoles for a set of frequencies. While the model values and measurements in general show similar trends, the measured correlation coefficients are systematically lower than the modeled value. This difference in model and measurements needs further investigation.

Acknowledgment

We acknowledge very useful discussions and suggestions from Matt Morgan during the initial phase of the development of the PAF model. The possibility of an analytical solution for PAF problem was pointed out to D. A. Roshi by Stuart Hay, CSIRO. We thank Marian Pospieszalski, Anthony Kerr for useful discussions on the noise properties of the receiver, Srikanth for discussions on the computation of the GBT aperture field, William Shillue for proofreading the manuscript and William Shillue, Robert Dickman and S. K. Pan for the support and useful discussions during the course of this work.

References

- [1] D. A. Roshi et al. Summary of january 2015 paf observations with the gbt, results and comparison with paf model. NRAO Electronic Division Internal Report 326, National Radio Astronomy Observatory (NRAO), 2015.
- [2] A. W. Hotan et al. The australian square kilometre array pathfinder: System architecture and specifications of the boolardy engineering test array. Publications of the Astronomical Society of the Pacific, September 2014. to be published.

- [3] G. Cortes-Medellin et al. A fully cryogenic phased array camera for radio astronomy. *IEEE Trans. Antennas Propag.*, 63:2471–2481, June 2015.
- [4] A. D. Gray et al. Activities of the dominion radio astrophysical observatory. In *General Assembly and Scientific Symposium, 2011 XXXth URSI XXXth*, pages 1–4, Istanbul, Turkey, August 2011.
- [5] T. Oosterloo et al. The latest on apertif. In *Proceedings of the ISKAF2010 Science Meeting*, pages 43–54, Assen, the Netherlands, June 2010.
- [6] J. R. Fisher. Phased array feed for low noise reflector antenna. NRAO Electronic Division Internal Report 307, National Radio Astronomy Observatory (NRAO), 1996.
- [7] K. F. Warnick et al. Minimizing the noise penalty due to mutual coupling for a receiving array. *IEEE Trans. Antennas Propag.*, 57:1634–1644, June 2009.
- [8] E. E. M. Woestenburg. Noise matching in dense phased arrays. Tech. Rep. RP-083, ASTRON, Dwingeloo, The Netherlands, 2005.
- [9] K. F. Warnick et al. Design and characterization of an active impedance matched low-noise phased array feed. *IEEE Trans. Antennas Propag.*, 59:1876–1885, June 2011.
- [10] S. G. Hay. Maximum-sensitivity matching of connected-array antennas subject to lange noise constants. *Int. Journal of Microw. and Optical Tech.*, 5:375–383, November 2010.
- [11] B. D. Jeffs et al. Signal processing for phased array feeds in radio astronomical telescopes. *IEEE Journal of Selected Topics in Signal Processing*, 2:635–646, October 2008.
- [12] J. E. Hudson. *Adaptive Array Principles*. Institute of Electrical Engineers, Stevenage, UK, 1981.
- [13] R. H. Clarke and J. Brown. *Diffraction Theory and Antennas*. Ellis Horwood Limited, Chichester, UK, 1980.
- [14] D. M. Pozar. *Microwave Engineering*. John Wiley and Sons, USA, 2005.
- [15] H. A. Haus et al. Representation of noise in linear twoports. *Proc. IRE*, 48:69–74, January 1960.
- [16] S. Weinreb et al. Matched wideband low-noise amplifiers for radio astronomy. *Review of Scientific Instruments*, 80:044702–5, April 2009.
- [17] P. Reich and W. Reich. A radio continuum survey of the northern sky at 1420 mhz. ii. *A&AS*, 63:205–291, February 1986.
- [18] R. Q. Twiss. Nyquist’s and thevenin’s theorems generalizaed for nonreciprocal linear networks. *J. Appl. Phys.*, 26(5):599–602, May 1955.
- [19] A. R. Kerr and J. Randa. Thermal noise and noise measurements – a 2010 update. *IEEE Microw. Mag.*, 11:40–52, October 2010.
- [20] B. M. Thomas. Theoretical performance of prime-focus paraboloids using cylindrical hybrid-mode feeds. *Proceedings of IEEE*, 118:1539–1549, November 1971.

- [21] M. W. Pospieszalski. Interpreting transistor noise. *IEEE Microw. Mag.*, 11:61–79, October 2010.
- [22] R. Hall and L. J. King. The green bank telescope. In *Antennas and Propagation Society International Symposium, 1992.*, pages 862–865, Chicago, USA, June 1992.
- [23] R. Norrid and S. Srikanth. A summary of the gbt optics. GBT memo 155, National Radio Astronomy Observatory (NRAO), 1996.

A Impedance matrix, Scattering matrix and Embedded beam pattern

A schematic of the PAF is shown in Fig. 1a. The impedance matrix \mathbf{Z} of PAF relates the port voltages, $\mathbf{V}^T = [v_1, v_2, \dots]$ and currents, $\mathbf{I}^T = [i_1, i_2, \dots]$,

$$\mathbf{V} = \mathbf{Z}\mathbf{I}. \quad (64)$$

This relationship can also be written in terms of the admittance matrix \mathbf{Y}

$$\mathbf{I} = \mathbf{Y}\mathbf{V}. \quad (65)$$

It follows from Eq. 64 and Eq. 65 that $\mathbf{Y} = \mathbf{Z}^{-1}$.

Another parameter that is used to describe network is Scattering matrix \mathbf{S} . This matrix relates the forward traveling wave $\mathbf{a} = [a_1, a_2, \dots]$ and the reverse traveling wave $\mathbf{b} = [b_1, b_2, \dots]$ (see Fig. 1a),

$$\mathbf{b} = \mathbf{S}\mathbf{a}. \quad (66)$$

The amplitude of the traveling waves and port voltages and currents are related through

$$\mathbf{V} = \sqrt{z_0}(\mathbf{a} + \mathbf{b}) \quad (67)$$

$$\mathbf{I} = \frac{1}{\sqrt{z_0}}(\mathbf{a} - \mathbf{b}) \quad (68)$$

where z_0 is the characteristic impedance of the transmission line. In this report we have taken $z_0 = 50 \Omega$, which is the reference impedance. Substituting these in Eq. 64 and keeping in mind that this equation holds for arbitrary set of \mathbf{a} we get

$$\mathbf{Z} = z_0(\mathcal{I} + \mathbf{S})(\mathcal{I} - \mathbf{S})^{-1} \quad (69)$$

Similarly the relationship between \mathbf{Y} and \mathbf{S} can be obtained as

$$\mathbf{Y} = \frac{1}{z_0}(\mathcal{I} - \mathbf{S})(\mathcal{I} + \mathbf{S})^{-1} \quad (70)$$

In Section 3.3, we defined the embedded beam pattern $\vec{\mathcal{E}}^e$. Here we present some characteristics of the embedded beam pattern and its relationship to impedance matrix.

1. The embedded beam pattern $\vec{\mathcal{E}}_i^e$ is the far-field pattern when the i^{th} input to the array is excited with a harmonic signal of 1 V peak value and all other inputs are short-circuited. For a loss less antenna,

$$\begin{aligned} \frac{1}{2z_f} \int_{sphere} \vec{\mathcal{E}}_i^e \cdot \vec{\mathcal{E}}_i^{e*} dA &= \frac{1}{2z_f} \int_{4\pi} \vec{E}_i^e \cdot \vec{E}_i^{e*} d\Omega \\ &= \frac{1}{2} i_{0_i}^2 \text{Re}\{Z_{pin_i}\} \end{aligned} \quad (71)$$

where z_f is the free space impedance, i_{0_i} is the current flowing to port i (see Fig. 1b) and Z_{pin_i} is the input impedance of port i when all other ports are short circuited. The input impedance for this case is given by

$$Z_{pin_i} = \frac{1}{Y_{ii}} \quad (72)$$

where Y_{ii} is the i^{th} diagonal element of the admittance matrix \mathbf{Y} . Thus, for 1 V excitation, $i_{0_i} = Y_{ii}$ in amps.

2. The open circuit voltage for embedded beam excitation (i.e. $v_{0_i} = 1$ V and 0 V for all other ports) can be obtained from Eq. 33 and Eq. 34 as

$$v_{oc_i} = z_{pin_i} \int_{A_{free}} \left(\vec{\mathcal{E}}^e \times \vec{\mathcal{H}}_r - \vec{\mathcal{E}}_r \times \vec{\mathcal{H}}^e \right) \cdot \hat{n} dA. \quad (73)$$

This equation is also true for any (loss-less) single port antenna, with z_{pin_i} as the input impedance of the antenna and $\vec{\mathcal{E}}^e$ as the beam pattern of the antenna when excited with 1 V.

3. The radiated power from the PAF for an arbitrary excitation can be written in terms of the embedded beam pattern. The radiated power P_{rad} is

$$\begin{aligned} P_{rad} &= \frac{1}{2z_f} \int_{sphere} \vec{\mathcal{E}} \cdot \vec{\mathcal{E}}^* dA \\ &= \frac{1}{2z_f} \int_{4\pi} \vec{E} \cdot \vec{E}^* d\Omega \end{aligned} \quad (74)$$

Using Eq. 35, Eq. 74 becomes

$$\begin{aligned} P_{rad} &= \frac{1}{2z_f} \int_{4\pi} \mathbf{V}_0^H \vec{E}^e \cdot \vec{E}^{eH} \mathbf{V}_0 d\Omega \\ &= \frac{1}{2z_f} \mathbf{V}_0^H \left(\int_{4\pi} \vec{E}^e \cdot \vec{E}^{eH} d\Omega \right) \mathbf{V}_0 \\ &= \frac{1}{2z_f} \mathbf{V}_0^H \mathbf{C}_{Ce} \mathbf{V}_0, \end{aligned} \quad (75)$$

where we define

$$\mathbf{C}_{Ce} \equiv \int_{4\pi} \vec{E}^e \cdot \vec{E}^{eH} d\Omega, \quad (76)$$

which is the correlation matrix of embedded beam patterns integrated over 4π solid angle.

4. For a loss-less antenna the power dissipated at the ports should be equal to the radiated power. Thus,

$$\begin{aligned}\frac{1}{2} \left(\frac{\mathbf{V}_0^H \mathbf{I}_0}{2} + \frac{\mathbf{I}_0^H \mathbf{V}_0}{2} \right) &= \frac{1}{2z_f} \mathbf{V}_0^H \mathbf{C}_{Ce} \mathbf{V}_0 \\ \frac{1}{4} \mathbf{V}_0^H \left(\mathbf{Z}^{-1} + (\mathbf{Z}^{-1})^H \right) \mathbf{V}_0 &= \frac{1}{2z_f} \mathbf{V}_0^H \mathbf{C}_{Ce} \mathbf{V}_0\end{aligned}\quad (77)$$

Since Eq. 77 holds for any \mathbf{V}_0 it follows

$$\begin{aligned}\frac{1}{2} \left(\mathbf{Z}^{-1} + (\mathbf{Z}^{-1})^H \right) &= \frac{1}{z_f} \mathbf{C}_{Ce} \\ &= \frac{1}{z_f} \int_{4\pi} \vec{\mathbf{E}}^e \cdot \vec{\mathbf{E}}^{eH} \, d\Omega\end{aligned}\quad (78)$$

B Spectral density at Thermal Equilibrium

To express the computed power spectral density in the report in terms of a physical temperature, it is necessary to know the spectral density when the array is in equilibrium with a black body radiation field of temperature T_0 and connected with noise-less receiver system. It follows from the first and second law of thermodynamics, that the correlation matrix of the open-circuit voltage at the output of antenna elements in the PAF is [18]

$$\mathbf{R}_t = \langle \mathbf{V}_{oc_t} \mathbf{V}_{oc_t}^H \rangle = 2k_B T_0 (\mathbf{Z} + \mathbf{Z}^H) \quad (79)$$

By applying the appropriate weights to this voltage correlation (see for example Eq. 10) we can obtain the power spectral density when the PAF is at thermal equilibrium. From the definition of noise figure[19], the conversion of any computed spectral density to a temperature is done by first dividing the spectral density with that when the PAF is in thermal equilibrium and then multiply by T_0 .

C Voltage correlation due to a thermal radiation field

We show here that the open circuit voltage correlation when the array is embedded in a black body radiation computed using Eq. 37 is identical to the result given by Twiss's theorem[18]. To do that we follow the arguments given in Section 3.4. For the case of the array embedded in a black body radiation field, the integral in Eq. 50 need to be extended to 4π solid angle. Thus the output voltage correlation \mathbf{R}_t becomes

$$\begin{aligned}\mathbf{R}_t &= \frac{4k_B T_0}{z_f} \mathbf{Z} \left(\int_{4\pi} \vec{\mathbf{E}}^e \cdot \vec{\mathbf{E}}^{eH} \, d\Omega \right) \mathbf{Z}^H, \\ &= \frac{4k_B T_0}{z_f} \mathbf{Z} \mathbf{C}_{Ce} \mathbf{Z}^H,\end{aligned}\quad (80)$$

where \mathbf{C}_{Ce} is defined by Eq. 76. Substituting Eq. 78 in Eq. 80 gives

$$\mathbf{R}_t = 2k_B T_0 (\mathbf{Z} + \mathbf{Z}^H), \quad (81)$$

which is the voltage correlation that follows from the laws of thermodynamics.

D Spillover temperature

To express the spillover noise in physical temperature we follow the prescription given in Appendix B,

$$T_{spill} = T_0 \frac{\mathbf{w}_1^H \mathbf{R}_{spill} \mathbf{w}_1}{\mathbf{w}_1^H \mathbf{R}_t \mathbf{w}_1} \quad (82)$$

$$= T_g \frac{\mathbf{w}_1^H \mathbf{Z} \left(\int_{\Omega_{spill}} \vec{\mathbf{E}}^e \cdot \vec{\mathbf{E}}^{eH} d\Omega \right) \mathbf{Z}^H \mathbf{w}_1}{\mathbf{w}_1^H \mathbf{Z} \left(\int_{4\pi} \vec{\mathbf{E}}^e \cdot \vec{\mathbf{E}}^{eH} d\Omega \right) \mathbf{Z}^H \mathbf{w}_1} \quad (83)$$

$$= T_g \frac{\mathbf{w}_1^H \mathbf{Z} \mathbf{C}_{Ce1} \mathbf{Z}^H \mathbf{w}_1}{\mathbf{w}_1^H \mathbf{Z} \mathbf{C}_{Ce} \mathbf{Z}^H \mathbf{w}_1} \quad (84)$$

where we used Eq. 80 for \mathbf{R}_t , Eq. 50 for \mathbf{R}_{spill} , and Eq. 76 and Eq. 51 define \mathbf{C}_{Ce} and \mathbf{C}_{Ce1} respectively. If we consider the antenna elements in the array are far apart such that \mathbf{Z} and the embedded beam correlations become diagonal matrices, then T_{spill} due to j^{th} antenna element can be obtained by considering the weight as 1 for j^{th} element and zeros for all other elements. In that case, Eq. 84 reduces to

$$T_{spill} = T_g \frac{\int_{\Omega_{spill}} \vec{\mathbf{E}}_j^e \cdot \vec{\mathbf{E}}_j^{e*} d\Omega}{\int_{4\pi} \vec{\mathbf{E}}_j^e \cdot \vec{\mathbf{E}}_j^{e*} d\Omega} = T_g (1 - \eta_{spill}). \quad (85)$$

Here we used the usual definition of spillover efficiency η_{spill} [20]. An alternate method to derive the result for a single port antenna is to start with Eq. 73 and follow the arguments in Section 3.4.

E Antenna temperature due to a source

Following the prescription given in Appendix B, the antenna temperature due to a source, T_A , can be written as

$$\begin{aligned} T_A &= \frac{\mathbf{w}_1^H \mathbf{R}_{signal} \mathbf{w}_1}{\mathbf{w}_1^H \mathbf{R}_t \mathbf{w}_1} T_0 \\ &= \frac{S_{source}}{2k_B} \frac{\mathbf{w}_1^H \mathbf{Z} \mathbf{C}_{Ie} \mathbf{Z}^H \mathbf{w}_1}{\mathbf{w}_1^H \mathbf{Z} \left(\int_{4\pi} \vec{\mathbf{E}}^e \cdot \vec{\mathbf{E}}^{eH} d\Omega \right) \mathbf{Z}^H \mathbf{w}_1} \\ &= \frac{S_{source}}{2k_B} \frac{\mathbf{w}_1^H \mathbf{Z} \mathbf{C}_{Ie} \mathbf{Z}^H \mathbf{w}_1}{\mathbf{w}_1^H \mathbf{Z} \mathbf{C}_{Ce} \mathbf{Z}^H \mathbf{w}_1} \\ &= \frac{S_{source} A_{ap} \eta_{ap}}{2k_B}. \end{aligned} \quad (86)$$

Here we used Eq. 53 for the signal correlation matrix \mathbf{R}_{signal} and Eq. 80 for the voltage correlation due to a black-body field \mathbf{R}_t . We define the aperture efficiency as

$$\eta_{ap} \equiv \frac{1}{A_{ap}} \frac{\mathbf{w}_1^H \mathbf{Z} \mathbf{C}_{Ie} \mathbf{Z}^H \mathbf{w}_1}{\mathbf{w}_1^H \mathbf{Z} \mathbf{C}_{Ce} \mathbf{Z}^H \mathbf{w}_1} \quad (87)$$

where A_{ap} is the aperture area of the telescope projected in the boresight direction. For antenna elements far apart and for weight 1 to j^{th} element and 0 to all other elements Eq. 87 reduces to

the usual definition[20]

$$\eta_{ap} = \frac{\left(\int_{A_{pap}} \vec{E}_{app,j}^e dA\right) \cdot \left(\int_{A_{pap}} \vec{E}_{app,j}^e dA\right)^*}{A_{ap} \int_{4\pi} \vec{E}_j^e \cdot \vec{E}_j^{e*} d\Omega} \quad (88)$$

We conjecture the following relationship

$$\mathbf{Z}(\mathbf{C}_{Ae} + \mathbf{C}_{ce1}) \mathbf{Z}^H = \mathbf{Z} \mathbf{C}_{ce} \mathbf{Z}^H. \quad (89)$$

where

$$\mathbf{C}_{Ae} \equiv \int_{A_{pap}} \vec{\mathcal{E}}_{app}^e \cdot \vec{\mathcal{E}}_{app}^{eH} dA. \quad (90)$$

Using Eq. 89, Eq. 86 can be written as

$$T_A = \frac{S_{source} A_{ap}}{2k_B} \frac{\mathbf{w}_1^H \mathbf{Z} \mathbf{C}_{Ie} \mathbf{Z}^H \mathbf{w}_1}{A_{ap} \mathbf{w}_1^H \mathbf{Z} \mathbf{C}_{Ae} \mathbf{Z}^H \mathbf{w}_1} \left(1 - \frac{\mathbf{w}_1^H \mathbf{Z} \mathbf{C}_{ce1} \mathbf{Z}^H \mathbf{w}_1}{\mathbf{w}_1^H \mathbf{Z} \mathbf{C}_{ce} \mathbf{Z}^H \mathbf{w}_1}\right). \quad (91)$$

We define the taper efficiency η_t as

$$\eta_t \equiv \frac{1}{A_{ap}} \frac{\mathbf{w}_1^H \mathbf{Z} \mathbf{C}_{Ie} \mathbf{Z}^H \mathbf{w}_1}{\mathbf{w}_1^H \mathbf{Z} \mathbf{C}_{Ae} \mathbf{Z}^H \mathbf{w}_1}. \quad (92)$$

To get the antenna temperature for a single antenna, we increase the distance between the elements so that matrices \mathbf{C}_{Ie} , \mathbf{C}_{Ae} , \mathbf{C}_{ce1} , \mathbf{C}_{ce} and \mathbf{Z} become diagonal and use weights 1 for one of the elements and 0 for all other elements. Eq. 91 then reduces to

$$T_A = \frac{S_{source} A_{ap} \eta_t \eta_{spill}}{2k_B} \quad (93)$$

where η_t and η_{spill} are the taper and spillover efficiencies in the usual definition[20].

F Receiver Temperature

Following the prescription in Appendix B, the receiver temperature of the PAF is

$$\begin{aligned} T_n &= T_0 \frac{\mathbf{w}_1^H \mathbf{R}_{rec} \mathbf{w}_1}{\mathbf{w}_1^H \mathbf{R}_t \mathbf{w}_1} \\ &= T_0 \frac{\mathbf{w}_1^H \left(R_n \mathcal{I} + \sqrt{R_n g_n} (\rho \mathbf{Z} + \rho^* \mathbf{Z}^H) + g_n \mathbf{Z} \mathbf{Z}^H \right) \mathbf{w}_1}{\frac{1}{2} \mathbf{w}_1^H (\mathbf{Z} + \mathbf{Z}^H) \mathbf{w}_1} \end{aligned} \quad (94)$$

where we used Eq. 60 for \mathbf{R}_{rec} and Eq. 79 for \mathbf{R}_t .

In radio astronomy instrumentation work[21] the receiver temperature T_n , versus source impedance for a single antenna connected to receiver is usually expressed as

$$T_n = T_{min} + NT_0 \frac{(Z_s - Z_{opt})(Z_s - Z_{opt})^*}{\text{Re}\{Z_s\} \text{Re}\{Z_{opt}\}} \quad (95)$$

where Z_s is the source impedance, and Z_{opt} is the optimum impedance. The minimum noise temperature, T_{min} , and N are Lange invariants of the amplifier. Z_{opt} and the Lange invariants are related to the noise parameters through expressions

$$\text{Im}\{Z_{opt}\} = \frac{\rho_i \sqrt{R_n g_n}}{g_n} \quad (96)$$

$$\text{Re}\{Z_{opt}\} = \frac{\sqrt{R_n g_n}}{g_n} \sqrt{1 - \rho_i^2} \quad (97)$$

$$N = \text{Re}\{Z_{opt}\} g_n \quad (98)$$

$$T_{min} = 2T_0 \left(N + \rho_r \sqrt{R_n g_n} \right) \quad (99)$$

We show below that Eq. 94 can be written in terms of the Lange invariants as

$$T_n = T_{min} + NT_0 \frac{\mathbf{w}_1^H (\mathbf{Z} - Z_{opt} \mathcal{I}) (\mathbf{Z} - Z_{opt} \mathcal{I})^H \mathbf{w}_1}{\text{Re}\{Z_{opt}\} \frac{1}{2} \mathbf{w}_1^H (\mathbf{Z} + \mathbf{Z}^H) \mathbf{w}_1} \quad (100)$$

Eq. 100 is a generalization of Eq. 95.

Equation 94 can be rewritten as

$$\begin{aligned} & \frac{1}{2} \mathbf{w}_1^H (\mathbf{Z} + \mathbf{Z}^H) \mathbf{w}_1 \frac{T_n}{T_0} \\ &= \mathbf{w}_1^H \left(R_n \mathcal{I} + \sqrt{R_n g_n} (\rho \mathbf{Z} + \rho^* \mathbf{Z}^H) + g_n \mathbf{Z} \mathbf{Z}^H \right) \mathbf{w}_1 \\ &= \mathbf{w}_1^H \left(2 \sqrt{R_n g_n} (1 - \rho_i^2) \text{Re}\{\mathbf{Z}\} + \right. \\ & \quad \left. 2 \rho_r \sqrt{R_n g_n} \text{Re}\{\mathbf{Z}\} \right) \mathbf{w}_1 + \\ & \quad \mathbf{w}_1^H \left(\frac{R_n g_n}{g_n} \mathcal{I} + g_n \mathbf{Z} \mathbf{Z}^H - 2 \sqrt{R_n g_n} (1 - \rho_i^2) \text{Re}\{\mathbf{Z}\} \right. \\ & \quad \left. - 2 \rho_i \sqrt{R_n g_n} \text{Im}\{\mathbf{Z}\} \right) \mathbf{w}_1 \\ &= 2 \left(\sqrt{R_n g_n} (1 - \rho_i^2) + \rho_r \sqrt{R_n g_n} \right) \frac{1}{2} \mathbf{w}_1^H (\mathbf{Z} + \mathbf{Z}^H) \mathbf{w}_1 + \\ & \quad \mathbf{w}_1^H \left(\frac{R_n g_n}{g_n} \mathcal{I} + g_n \mathbf{Z} \mathbf{Z}^H - 2 \sqrt{R_n g_n} (1 - \rho_i^2) \text{Re}\{\mathbf{Z}\} \right. \\ & \quad \left. - 2 \rho_i \sqrt{R_n g_n} \text{Im}\{\mathbf{Z}\} \right) \mathbf{w}_1 \\ &= \frac{T_{min}}{T_0} \frac{1}{2} \mathbf{w}_1^H (\mathbf{Z} + \mathbf{Z}^H) \mathbf{w}_1 + \\ & \quad \mathbf{w}_1^H \left(g_n |Z_{opt}|^2 \mathcal{I} + g_n \mathbf{Z} \mathbf{Z}^H - 2 g_n \text{Re}\{Z_{opt}\} \text{Re}\{\mathbf{Z}\} \right. \\ & \quad \left. - 2 g_n \text{Im}\{Z_{opt}\} \text{Im}\{\mathbf{Z}\} \right) \mathbf{w}_1 \\ &= \frac{T_{min}}{T_0} \frac{1}{2} \mathbf{w}_1^H (\mathbf{Z} + \mathbf{Z}^H) \mathbf{w}_1 + \\ & \quad g_n \mathbf{w}_1^H (\mathbf{Z} - Z_{opt} \mathcal{I}) (\mathbf{Z} - Z_{opt} \mathcal{I})^H \mathbf{w}_1 \\ &= \frac{T_{min}}{T_0} \frac{1}{2} \mathbf{w}_1^H (\mathbf{Z} + \mathbf{Z}^H) \mathbf{w}_1 + \\ & \quad N \frac{\mathbf{w}_1^H (\mathbf{Z} - Z_{opt} \mathcal{I}) (\mathbf{Z} - Z_{opt} \mathcal{I})^H \mathbf{w}_1}{\text{Re}\{Z_{opt}\}} \end{aligned} \quad (101)$$

Eq. 101 can be readily rewritten as Eq. 100.

G CST Far-field pattern, Scattering Matrix and Energy Balance

As described in Section 4.1 the Scattering matrix and Far-field pattern of the PAF are obtained using CST software package. The Scattering matrix when exported in TOUCHSTONE format is normalized to a reference impedance of 50Ω . CST computes the far-field pattern by exciting the i^{th} array element and keeping all other ports terminated with the transmission line impedance, which in our case is 50Ω . These field patterns, referred to as \vec{E}'_i , depends only on (θ, ϕ) and are in units of V. The field values are provided for a (default) reference distance r of 1 m. Since all array elements are not located at the co-ordinate origin, a geometric phase will be present in the far-field pattern. The field patterns \vec{E}'_i provided by CST includes this geometric phase factor.

We check here whether the simulation results satisfies the energy balance. The peak power used in CST simulation is 1 W, which corresponds to a RMS (root mean square) power, P_{stim} of 0.5 W for sinusoidal excitation. The amplitude of traveling waves \mathbf{a} when j^{th} port is excited is

$$\begin{aligned} a_i &= \sqrt{2P_{stim}} \quad \text{for } i = j \\ &= 0 \quad \text{for } i \neq j \end{aligned} \quad (102)$$

where a_i are elements of vector \mathbf{a} . The reflected wave vector \mathbf{b} is given by Eq. 66. The total reflected power $P_{reflect}$, which is dissipated in the port impedance, is

$$P_{reflect} = \frac{1}{2} \mathbf{b}^H \mathbf{b} = \frac{1}{2} \mathbf{a}^H \mathbf{S}^H \mathbf{S} \mathbf{a} \quad (103)$$

The total radiated power P_{rad} is

$$P_{rad} = \frac{1}{2z_f} \int_{4\pi} \vec{E}'_i \vec{E}'_i^* d\Omega \quad (104)$$

A plot of $P_{rad} + P_{reflect}$ for the 38 dipoles and for frequencies in the range 1.0 to 2.0 GHz is shown in Fig. 14. As seen from the plot, the calculated total power is equal to 0.5 W.

H Embedded beam patterns from CST far-field patterns

CST provides far-field pattern when j^{th} port is excited and all other ports are terminated with port impedance (i.e. 50Ω). Using Eq. 35,

$$\vec{E}'_j = \sum_{i=1, M} q_{ij} \vec{E}_i^e, \quad (105)$$

here $q_{ij} = v_{0_i}$ are the port voltages under the excitation condition said above. These voltages can be computed using the Scattering Matrix. The elements of wave amplitude vector for the excitation is

$$\begin{aligned} a_i &= \sqrt{2P_{stim}} \quad \text{for } i = j \\ &= 0 \quad \text{for } i \neq j \end{aligned} \quad (106)$$

The wave amplitude vector \mathbf{b} is then

$$\mathbf{b} = a_j \begin{bmatrix} S_{1j} \\ S_{2j} \\ \vdots \\ S_{jj} \\ \vdots \\ S_{Mj} \end{bmatrix}, \quad (107)$$

where a_j is the j^{th} element of the vector \mathbf{a} , S_{ij} , $i = 1$ to M is the j^{th} column of \mathbf{S} . The port voltage is then

$$\begin{aligned} q_{ij} &= \sqrt{z_0}(a_i + b_i) \\ &= \sqrt{z_0}(1 + S_{jj})a_j \quad \text{for } i = j \\ &= \sqrt{z_0}S_{ij}a_j \quad \text{for } i \neq j \end{aligned} \quad (108)$$

The set of far-field patterns provided by CST along with the port voltage can be used to obtain the embedded beam pattern. Eq. 105 for the set of far-field patterns can be concisely written as

$$\vec{\mathbf{E}}' = \mathbf{Q} \vec{\mathbf{E}}^e, \quad (109)$$

where the elements of \mathbf{Q} are q_{ij} . This equation is valid for each θ, ϕ . Using Eq. 108 \mathbf{Q} can be written as

$$\mathbf{Q} = \sqrt{2z_0 P_{stim}} (\mathbf{I} + \mathbf{S}). \quad (110)$$

The embedded beam patterns are then given by

$$\vec{\mathbf{E}}^e = \mathbf{Q}^{-1} \vec{\mathbf{E}}', \quad (111)$$

Fig. 15 shows some example plots of CST far-field patterns and the computed embedded beam patterns.

Some sanity checks on the computed embedded beam patterns are done below. We computed the radiated power using the embedded beam pattern (Eq. 75) and compared with those obtained using Eq. 104. The two radiated powers have identical values.

Second we check whether the embedded beam pattern satisfy the energy conservation. By definition of embedded beam pattern we excite the array with 1 V peak at port j and short circuit all other ports. Thus

$$v_{0_i} = 1 \quad \text{for } i = j \quad (112)$$

$$= 0 \quad \text{for } i \neq j. \quad (113)$$

The wave amplitudes are then

$$\sqrt{z_0}(a_i + b_i) = 1 \quad \text{for } i = j \quad (114)$$

$$\sqrt{z_0}(a_i + b_i) = 0 \quad \text{for } i \neq j \quad (115)$$

$$(116)$$

The vector \mathbf{a} can be written as

$$\mathbf{a} = -\mathbf{b} + \frac{1}{\sqrt{z_0}} \begin{bmatrix} 0 \\ 0 \\ \vdots \\ 1 \\ \vdots \\ 0 \end{bmatrix} \quad (117)$$

where the non-zero element (which is 1) is located at j^{th} row. Substituting in Eq. 66 and rearranging we get

$$\mathbf{b} = \frac{1}{\sqrt{z_0}}(\mathcal{I} + \mathbf{S})^{-1} \begin{bmatrix} S_{1j} \\ S_{2j} \\ \vdots \\ S_{jj} \\ \vdots \\ S_{Mj} \end{bmatrix}. \quad (118)$$

Power dissipated at the j^{th} port is

$$P_{dis} = \frac{1}{2}(a_j a_j^* - b_j b_j^*) \quad (119)$$

$$= \frac{1}{2\sqrt{z_0}}\left(\frac{1}{\sqrt{z_0}} - (b_j + b_j^*)\right) \quad (120)$$

Another method to get P_{dis} is by using Eq. 71 and Eq. 72;

$$P_{dis} = \frac{1}{2}\text{Re}\{Y_{jj}\} \quad (121)$$

The radiated power computed from embedded beam patterns are found to be equal to P_{dis} (see Fig. 16).

I Computation of spillover integral, aperture field and aperture field integral

The integrals in Eq. 51 and Eq. 54 are evaluated using the coordinate system described here. We also briefly describe the computation of aperture field for the evaluation of Eq. 54.

The geometry of the GBT is discussed in [22], [23]. The GBT surface is cut from a parent symmetric paraboloid of diameter 208 m and f/D of 0.29. Here f = 60 m is the focal length and D = 208 m is the diameter of the parent paraboloid. The equation of the parent paraboloid is

$$z_{pp} = f - \frac{x_{pp}^2 + y_{pp}^2}{4f}. \quad (122)$$

The coordinate system $x_{pp} - y_{pp} - z_{pp}$ is shown in Fig. 17. The GBT surface is obtained by the intersection of a plane at $\sim 24^\circ$ with the parent paraboloid. The coordinates in m of the intersection of the plane at $x_{pp} = 0$ are (0, -4.0, 59.933) and (0, -104, 14.933) corresponding to the top and bottom end of the GBT surface respectively.

The PAF field patterns are obtained with respect to the coordinate system $x_p - y_p - z_p$, which is same as the $x - y - z$ coordinated in the CST (see Fig. 5). The $x_p - y_p$ are rotated by 45° with respect to the $X - Y$ axis shown in Fig. 4 as well as the $u - v$ co-ordinates of the CST. The x and y polarization dipoles are aligned along the x_p and y_p axis respectively (see Fig. 4). The PAF is mounted on the GBT such that z_p passes through the projected center of the aperture plane on the GBT surface. The co-ordinates of the projected center are (0, -54.0, 47.85) in m. The angle between z_{pp} and z_p is 48.46° , which is referred to as the feed angle β . Since the X axis shown in Fig. 4 is parallel to elevation axle, the orientation of the $x_p - y_p$ with respect to $x_{pp} - y_{pp} - z_{pp}$ is obtained first by rotating the $x_p - y_p$ by 45° clockwise with respect to $x_{pp} - y_{pp}$ and then rotating the z_p axis by angle β with respect to z_{pp} .

The boresight coordinates $x_b - y_b - z_b$ and $x_{pp} - y_{pp} - z_{pp}$ coordinates are related through the transformation

$$\mathbf{PP2B} = \begin{bmatrix} \cos(\pi/4), -\sin(\pi/4), 0 \\ -\sin(\pi/4), -\cos(\pi/4), 0 \\ 0, 0, -1 \end{bmatrix}. \quad (123)$$

The rotation of the $x_b - y_b$ coordinates by 45° will essentially align the x and y polarization of the aperture field with these coordinate axes. The source coordinates are rotated by θ_s, ϕ_s with respect to the boresight coordinates. The coordinates of the projected aperture plane in the direction of source are obtained by defining a plane perpendicular to the unit vector $\hat{u}_z = \cos(\phi_s)\sin(\theta_s)\hat{i}_b + \sin(\phi_s)\sin(\theta_s)\hat{j}_b + \cos(\theta_s)\hat{k}_b$, where $\hat{i}_b, \hat{j}_b, \hat{k}_b$ are the unit vectors along the x_b, y_b, z_b axes.

The aperture field is obtained using Geometric optics. We also assume that the GBT surface is a perfect conductor. The boundary condition during reflection is that the tangential component of the field at the surface is zero,

$$\vec{\mathcal{E}}_i^{e(i)} - \hat{r}_n \cdot \vec{\mathcal{E}}_i^{e(i)} \hat{r}_n = -\vec{\mathcal{E}}_i^{e(r)} + \hat{r}_n \cdot \vec{\mathcal{E}}_i^{e(r)} \hat{r}_n, \quad (124)$$

where $\vec{\mathcal{E}}_i^{e(i)}$ and $\vec{\mathcal{E}}_i^{e(r)}$ are the incident and reflected fields respectively and \hat{r}_n is the unit normal to the surface element where reflection is taking place. Since the surface is assumed to be loss-less $|\vec{\mathcal{E}}_i^{e(i)}| = |\vec{\mathcal{E}}_i^{e(r)}|$. Applying Snell's law it follows that

$$\vec{\mathcal{E}}_i^{e(r)} = 2\hat{r}_n \cdot \vec{\mathcal{E}}_i^{e(i)} \hat{r}_n - \vec{\mathcal{E}}_i^{e(i)} \quad (125)$$

The unit normal is given by

$$\begin{aligned} \hat{r}_n &= -\frac{\vec{r}_\theta \times \vec{r}_\phi}{|\vec{r}_\theta \times \vec{r}_\phi|} \\ &= -\cos(\theta_{pp}/2)\hat{r}_{pp} + \sin(\theta_{pp}/2)\hat{\theta}_{pp}, \end{aligned} \quad (126)$$

where $\vec{r}_\theta = \frac{\partial \vec{r}_{pp}}{\partial \theta_{pp}}$, $\vec{r}_\phi = \frac{\partial \vec{r}_{pp}}{\partial \phi_{pp}}$ and $(|\vec{r}_{pp}|, \theta_{pp}, \hat{\theta}_{pp}, \phi_{pp}, \hat{\phi}_{pp})$ are spherical coordinates of the GBT surface in the $x_{pp} - y_{pp} - z_{pp}$ system. The incident fields are the beam patterns provided by the CST scaled by the distance from the focus to the reflector. The reflected field is propagated to the source coordinate to get the aperture field, which is given by $\vec{\mathcal{E}}_i^{e(r)} e^{-\frac{j2\pi(2f+z_b^s)}{\lambda}}$, where z_b^s is the z component of the project aperture plane in the boresight coordinates.

J Symbols and Notations used in this report

The bold letters represent $m \times n$, $1 \times n$ and $m \times 1$ matrices (example \mathbf{M}). The $1 \times n$ and $m \times 1$ matrices are referred to as vectors. Transpose of a matrix is represented, for example, by \mathbf{M}^T and Hermitian transpose is represented, for example, by \mathbf{M}^H . Complex conjugate of variable say v is denoted by v^* . Vectors in real space are represented with an arrow on the top of non-bold symbol (example \vec{E}). An arrow on top of a bold symbol is used to represent a matrix or vector of real space vectors (example $\vec{\mathbf{E}}$). For example,

$$\vec{\mathbf{E}}^T = [\vec{\mathcal{E}}_1^e, \vec{\mathcal{E}}_2^e, \dots]$$

The calligraphic symbols are used to represent *electromagnetic fields* which depends on the position vector \vec{r} (example $\vec{\mathcal{E}}^e$) and Latin symbols are used for *electromagnetic fields* which depends on the

angular coordinates θ, ϕ (example \vec{E}^e). The operation $\vec{\mathcal{E}}^e \times \mathcal{I} \vec{\mathcal{H}}_r$ can be expanded as

$$\begin{bmatrix} \vec{\mathcal{E}}_1^e, \vec{\mathcal{E}}_2^e, \dots, \vec{\mathcal{E}}_M^e \end{bmatrix} \times \begin{bmatrix} 1, 0, 0, \dots \\ 0, 1, 0, \dots \\ \vdots \\ \dots, 0, 1 \end{bmatrix} \vec{\mathcal{H}}_r = \begin{bmatrix} \vec{\mathcal{E}}_1^e \times \vec{\mathcal{H}}_r \\ \vec{\mathcal{E}}_2^e \times \vec{\mathcal{H}}_r \\ \vdots \\ \vec{\mathcal{E}}_M^e \times \vec{\mathcal{H}}_r \end{bmatrix}$$

Similarly the operation $\mathbf{Z} \mathcal{I} \hat{p} \cdot \vec{\mathcal{E}}^e$ can be expanded as

$$\mathbf{Z} \begin{bmatrix} \hat{p}, 0, 0, \dots \\ 0, \hat{p}, 0, \dots \\ \vdots \\ \dots, 0, \hat{p} \end{bmatrix} \cdot \begin{bmatrix} \vec{\mathcal{E}}_1^e \\ \vec{\mathcal{E}}_2^e \\ \vdots \\ \vec{\mathcal{E}}_M^e \end{bmatrix} = \begin{bmatrix} z_{11}, z_{12}, \dots, z_{1M} \\ z_{21}, z_{22}, \dots, z_{2M} \\ \vdots \\ z_{M1}, z_{M2}, \dots, z_{MM} \end{bmatrix} \begin{bmatrix} \vec{\mathcal{E}}_1^e \cdot \hat{p} \\ \vec{\mathcal{E}}_2^e \cdot \hat{p} \\ \vdots \\ \vec{\mathcal{E}}_M^e \cdot \hat{p} \end{bmatrix}$$

η_{ap}	Aperture efficiency
η_{tap}	Taper efficiency
η_{spill}	Spillover efficiency
λ	Free space wavelength of radiation
θ_s, ϕ_s	Source position in the sky w.r.t the boresight coordinate system
$a_i, b_i, \mathbf{a}, \mathbf{b}$	Traveling wave amplitudes in the transmission line
\mathbf{A}	Matrix that transform open-circuit voltage to 'loaded' voltage
A	Enclose area in Lorentz integral (Eq. 24)
A_{ap}	Physical area of the telescope aperture projected in the boresight direction
A_{trans}	Cross section area in the transmission line (see Fig. 2)
A_{free}	Surface area away from the metallic surface of the PAF (see Fig. 2)
c	Velocity of light in free space
D_{array}	Maximum physical size of the PAF
$\vec{\mathcal{E}}^e, \vec{E}^e$	Embedded electric field patterns
$\vec{\mathcal{E}}^e, \vec{E}^e$	Set of M embedded electric field patterns
$\vec{\mathcal{E}}_{pap}^e$	Set of M embedded electric field patterns propagated to the aperture plane projected in the direction of the source
$\vec{\mathcal{E}}_{pap,x}^e, \vec{\mathcal{E}}_{pap,y}^e$	x and y components of $\vec{\mathcal{E}}_{pap}^e$
e_{max}	Maximum eigenvalue of system characteristics matrix
\mathbf{G}	Gain matrix of the system (diagonal)
$\vec{\mathcal{H}}^e, \vec{H}^e$	Embedded magnetic field patterns
$\vec{\mathcal{H}}^e, \vec{H}^e$	Set of M embedded magnetic field patterns
$\vec{\mathcal{H}}_{pap}^e$	Set of M embedded magnetic field patterns propagated to the aperture plane projected in the direction of the source
i_{0_i}, \mathbf{I}_0	Excitation current for the PAF (source impedance = z_0)
\mathcal{I}	Identity matrix
k	Wave vector of spherical waves of radiation pattern
k_B	Boltzmann constant
k_{inc}	Wave vector of the incident radiation field (plane wave and also arbitrary wave front)
M	number of elements in the PAF

M	Characteristics matrix of the system (i.e. PAF+telescope+receiver)
N	Open-circuit voltage correlation matrix of the total noise at the output of the antenna array
\hat{p}	Unit vector along the polarization of an incident radiation
P_{rad}	Power radiated by the PAF
$P_{reflect}$	Power reflected from the ports of the PAF
P_{stim}	Excitation power used by CST 1 W peak-peak
\vec{r}, r	Position vector and its magnitude
R_n, g_n, ρ	Noise resistance, conductance of the low-noise amplifier and their correlation coefficient
\tilde{R}	Correlation of ‘loaded’ voltages
R	Correlation of open-circuit voltages
R_t	Correlation of open-circuit voltages at the output of the antenna array when it is enclosed in a black body radiation field
S	Scattering matrix
S_{source}	Flux density of source
SNR	signal-to-noise ratio
T_A	Antenna temperature
T_{sys}	System temperature
T_g	Physical temperature of the ground
T_0	Reference temperature 290 K
T_{cmb}	Cosmic microwave background temperature
T_{sky}	Brightness temperature of sky background radiation at the frequency of interest
v_{0i}, V_0	Excitation voltage for the PAF (source impedance = z_0)
\tilde{V}	‘Loaded’ voltage at the input of the beamformer or combiner
V_{oc}	Open-circuit voltage at the output of the antenna array
w, w_1, w_2	Weight vectors
x_b, y_b, z_b	Boresight coordinate system
x_p, y_p, z_p	Coordinate system on the PAF which is used to obtain the radiation pattern. In Fig. 5, this is shown as the u-v-w coordinates.
x, y, z	Coordinate system with z-axis pointing towards the source
Y	Admittance matrix of the PAF
z_0	Reference impedance 50 Ω , also characteristic impedance of the transmission line
z_f	Free space impedance
Z	Impedance matrix of the PAF
Z_{in}	input impedance of the low-noise amplifier
Z_{in}	input impedance (diagonal) matrix
Z_{pini}	Input impedance of a port of the PAF when all other ports are short circuited

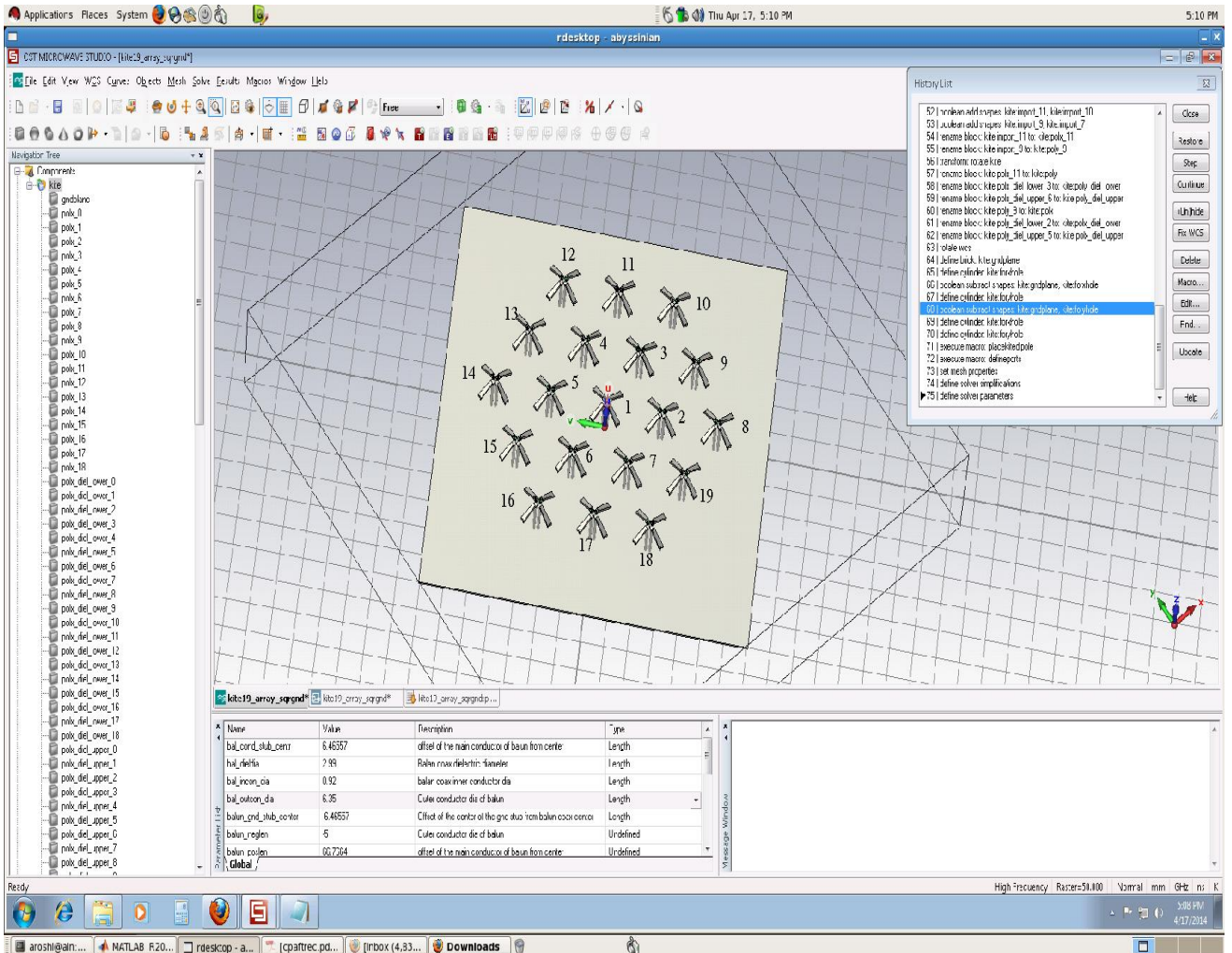


Figure 5: 19-element Kite Array Mode in CST. The far-field patterns are computed with respect to the x-y-z co-ordinate system. The origin of this system is located at the intersection of ground plane and dipole 1.

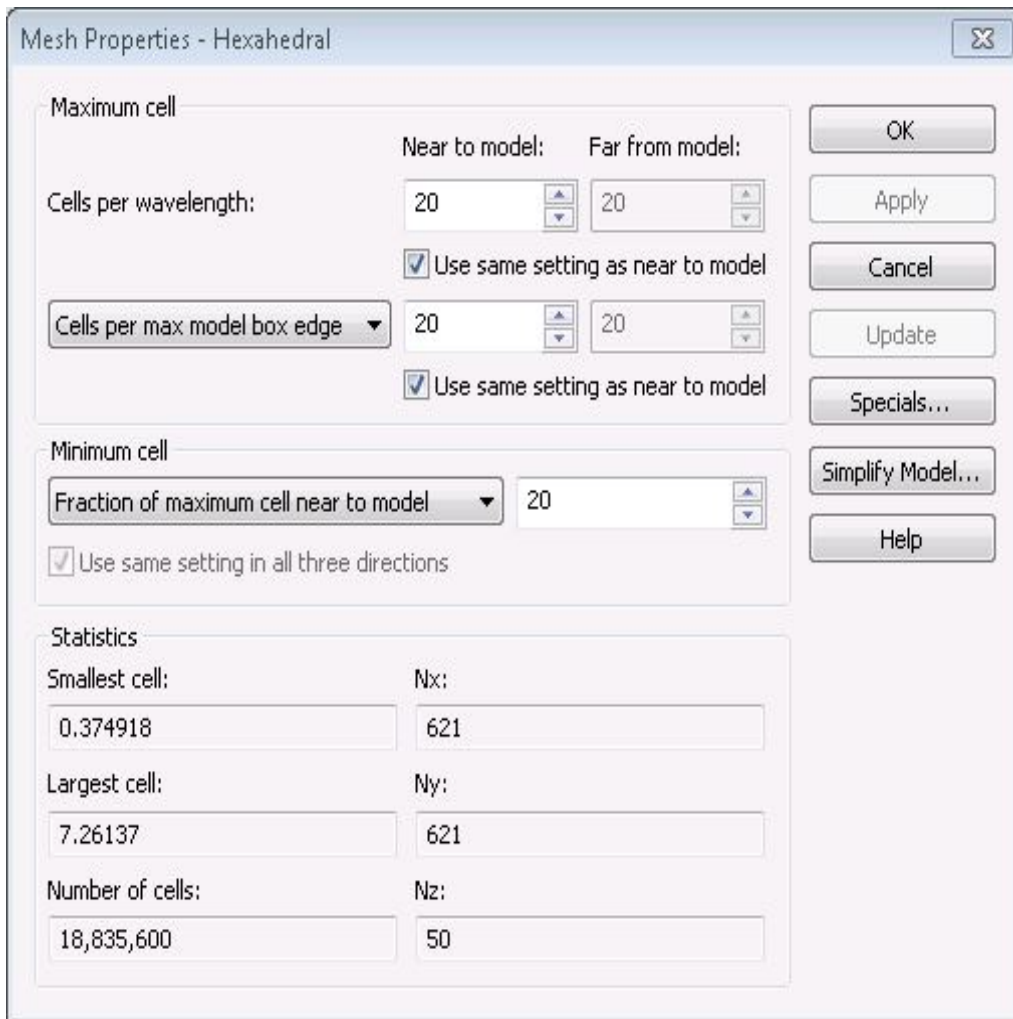


Figure 6: Mesh parameters used for the simulation in CST.

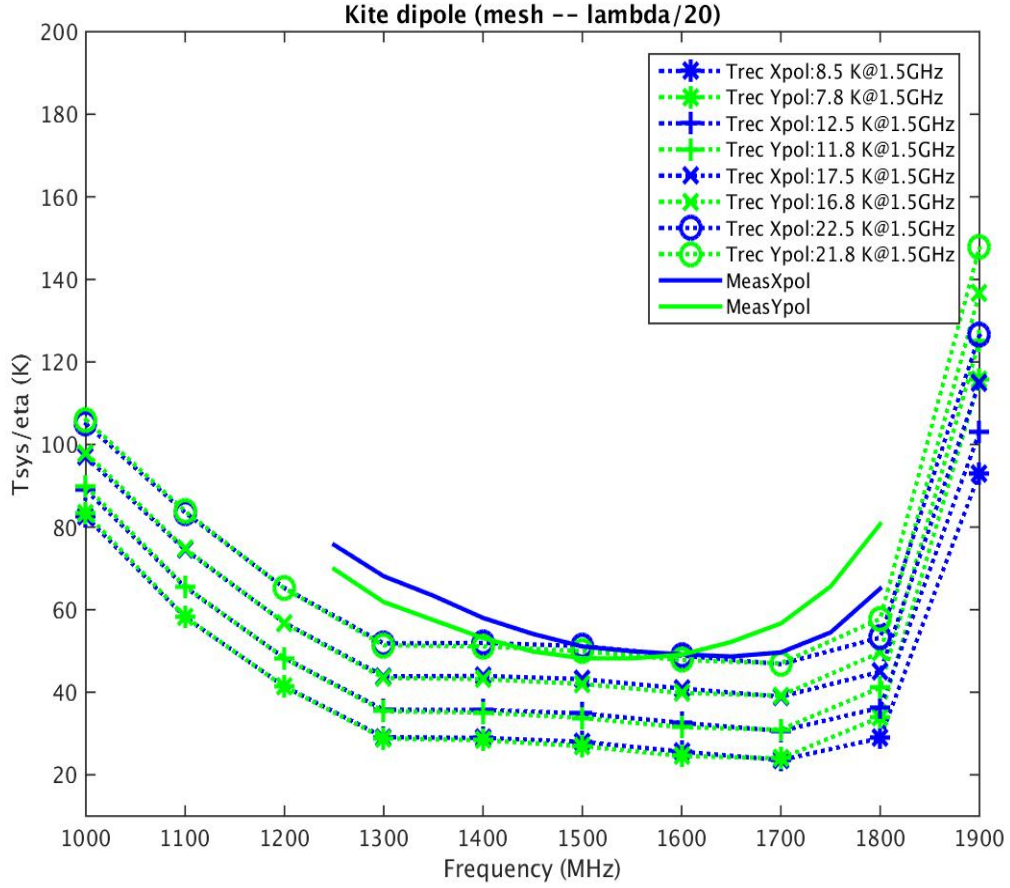


Figure 7: $\frac{T_{sys}}{\eta}$ vs frequency from Virgo A observations (solid line) and PAF model (dotted line). The model $\frac{T_{sys}}{\eta}$ is calculated for different receiver temperature (see text for details). The receiver temperature of each set of models at 1.5 GHz is marked on the plot.

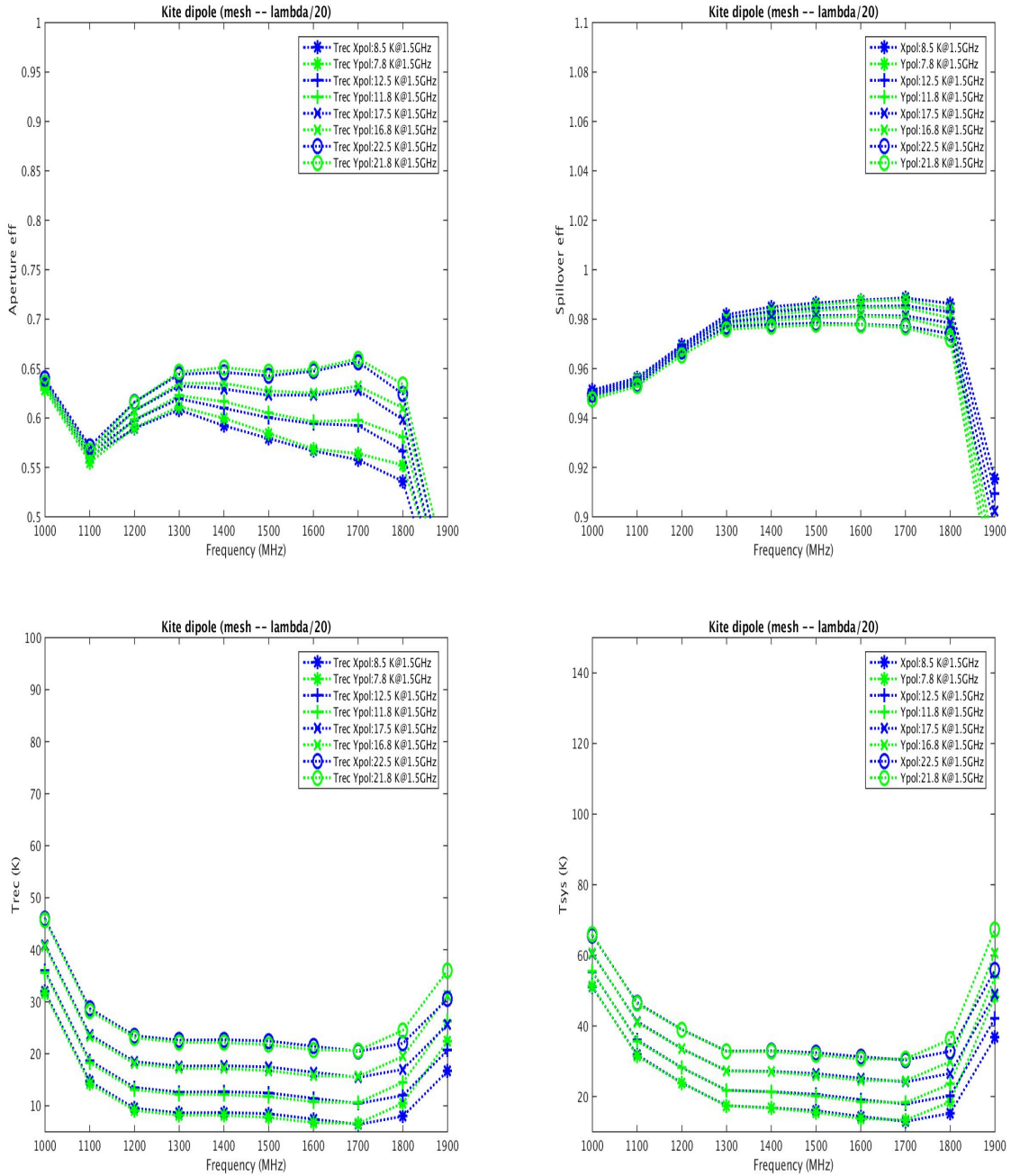


Figure 8: Model aperture efficiency (top right), spillover efficiency (top left), receiver temperature (bottom right) and system temperature (bottom left) vs frequency. The receiver temperature of each set of models at 1.5 GHz is marked on the plot.

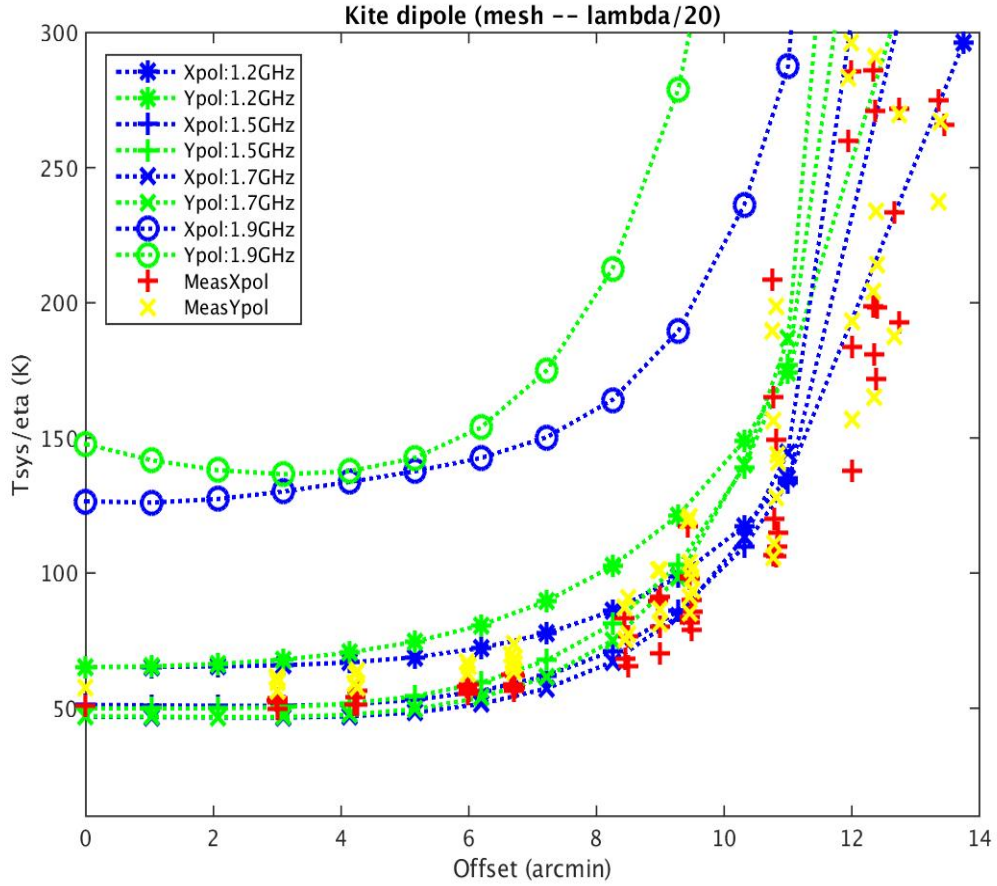


Figure 9: $\frac{T_{sys}}{\eta_{ap}}$ vs offset from boresight direction from Virgo A ‘grid’ observations (+ & x points) and PAF model (dotted line). The model $\frac{T_{sys}}{\eta_{ap}}$ is calculated for receiver temperature ~ 22 K at 1.5 GHz. The model values are plotted for different frequencies as marked on the plot. The measurements are made at 1.7 GHz.

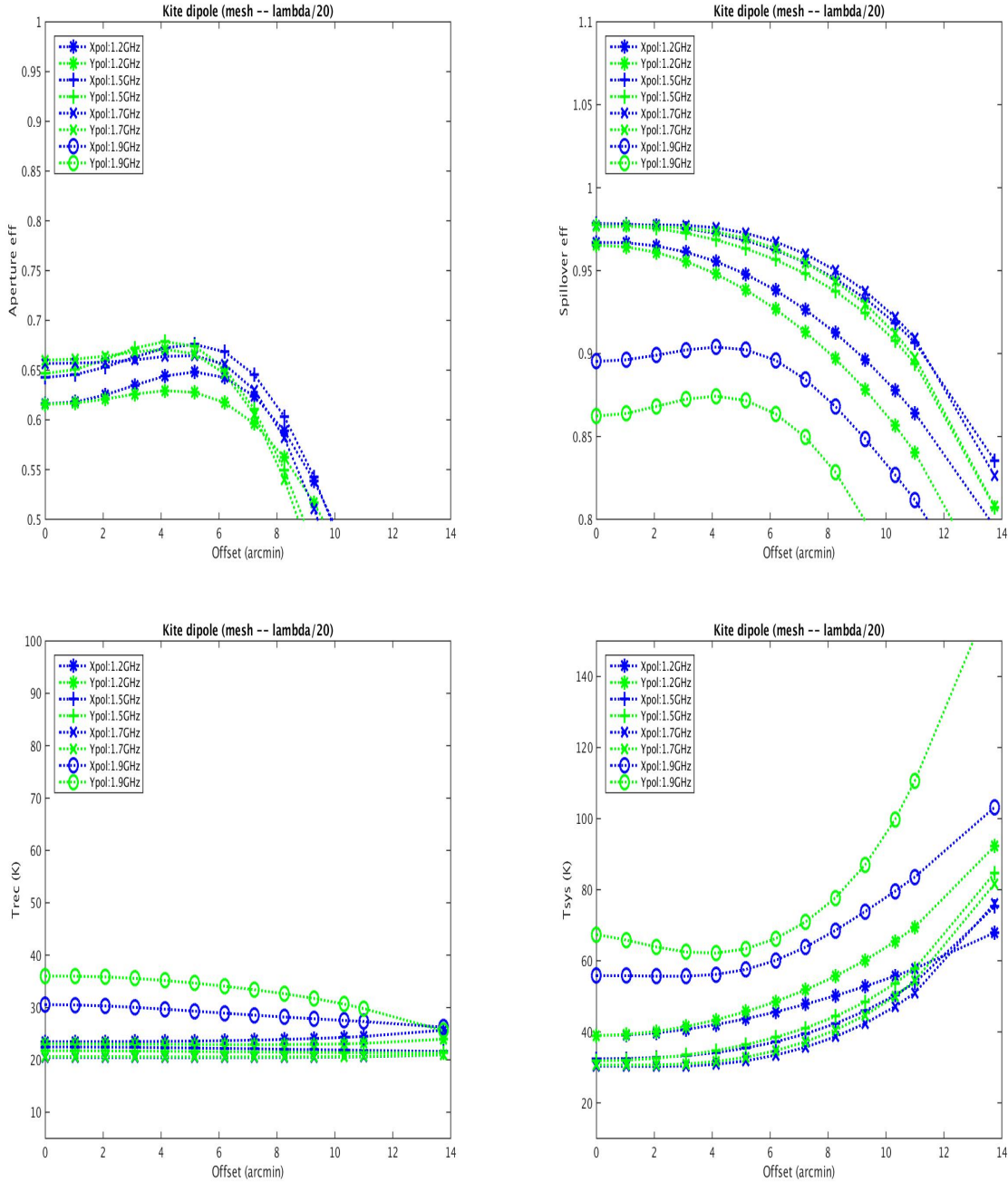


Figure 10: Model aperture efficiency (top right), spillover efficiency (top left), receiver temperature (bottom right) and system temperature (bottom left) vs offset from boresight direction. The receiver temperature for the models is ~ 22 K at 1.5 GHz. Model values for different frequencies are plotted as marked on the plots

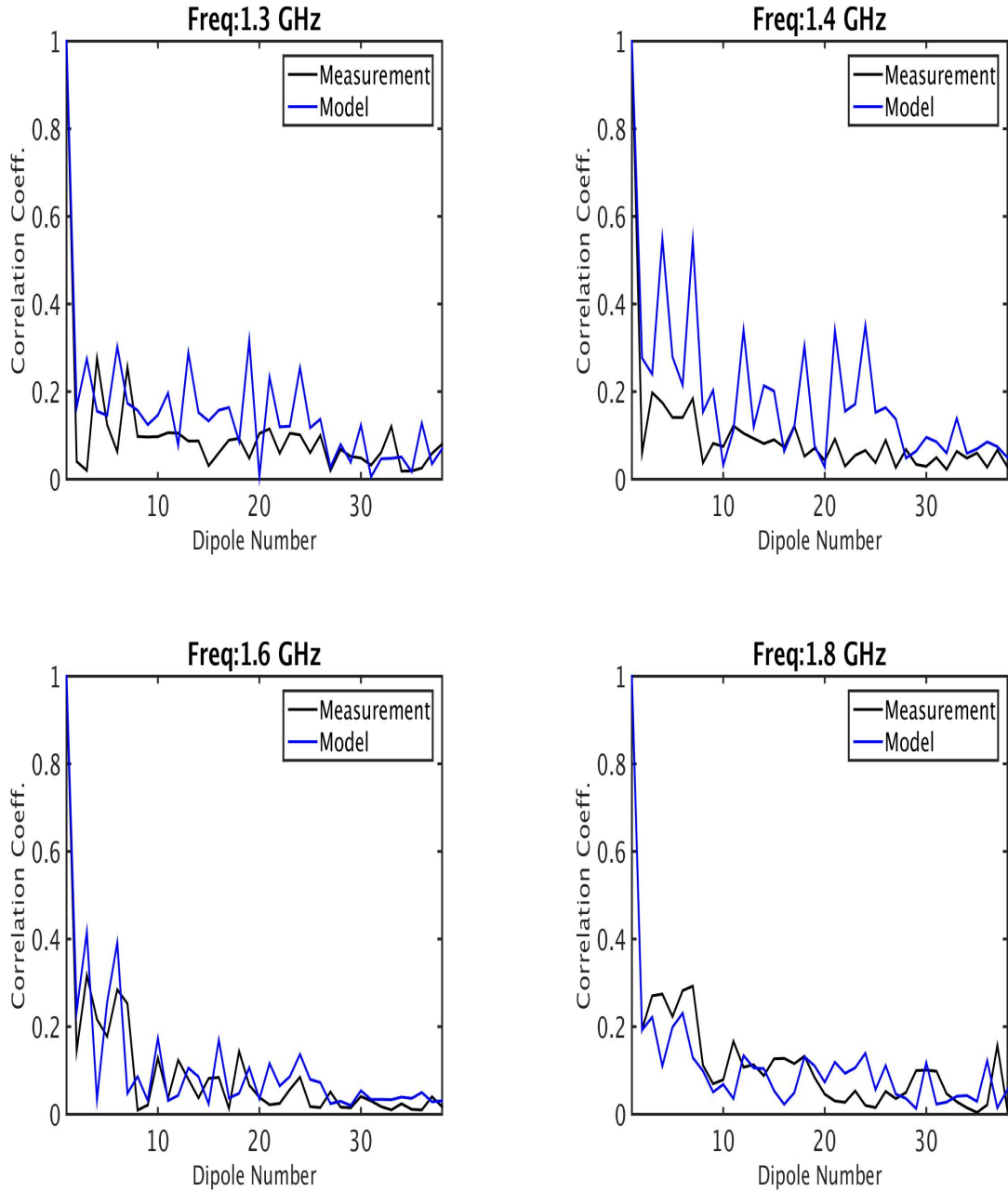


Figure 11: Model noise correlations (blue) and measured correlations (black) between dipole 1 and other dipoles. Dipoles 1 to 19 correspond to X polarization and 20 to 38 correspond to Y polarization. The frequencies at which the correlations are obtained are marked on the plot.

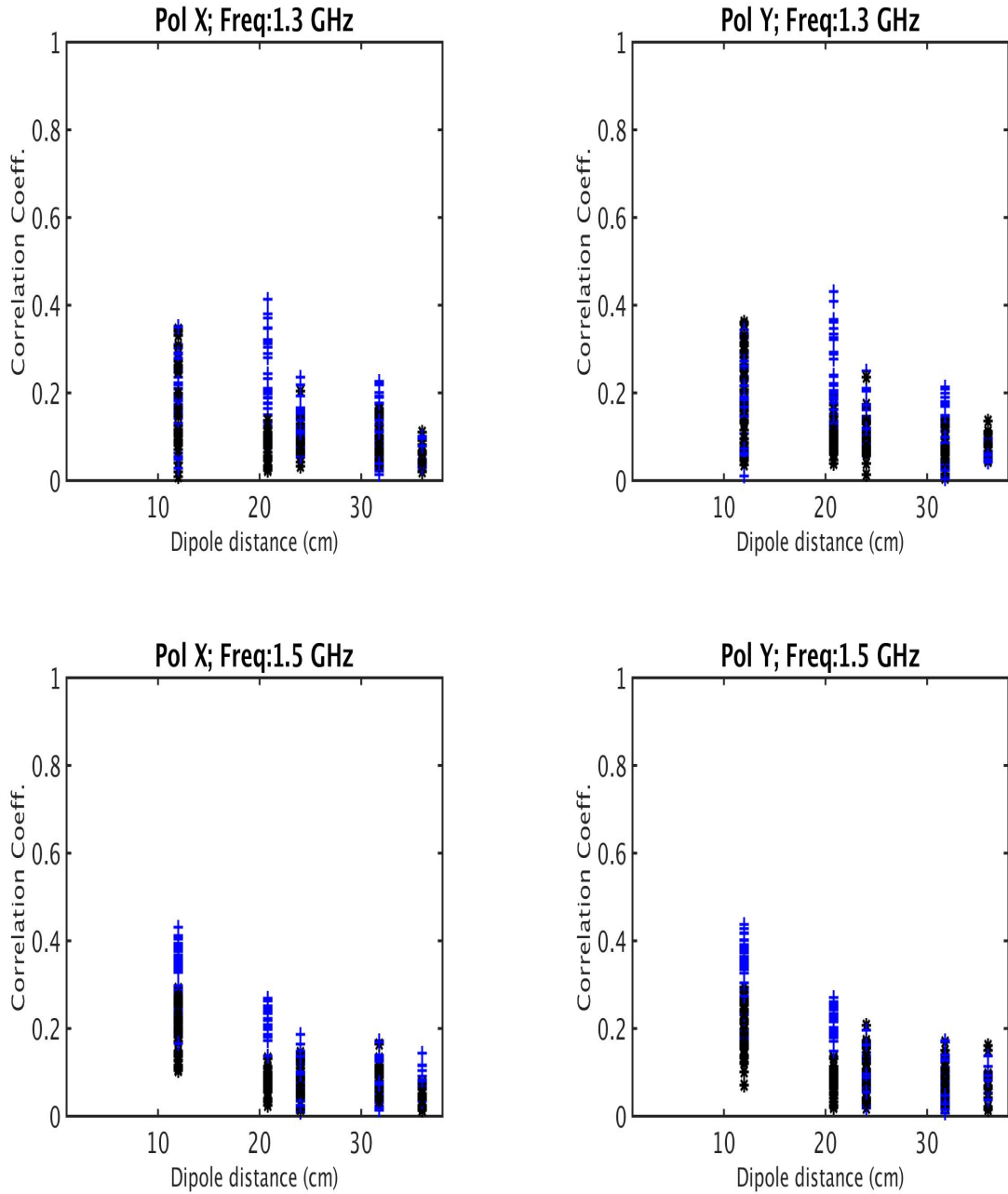


Figure 12: Model noise correlations (blue) and measured correlations (black) between dipoles vs relative separation of dipoles in PAF. The correlations from X polarization dipole are shown on the right and those from Y polarization dipole are shown on the left. The frequencies at which the correlations are obtained are marked on the plot.

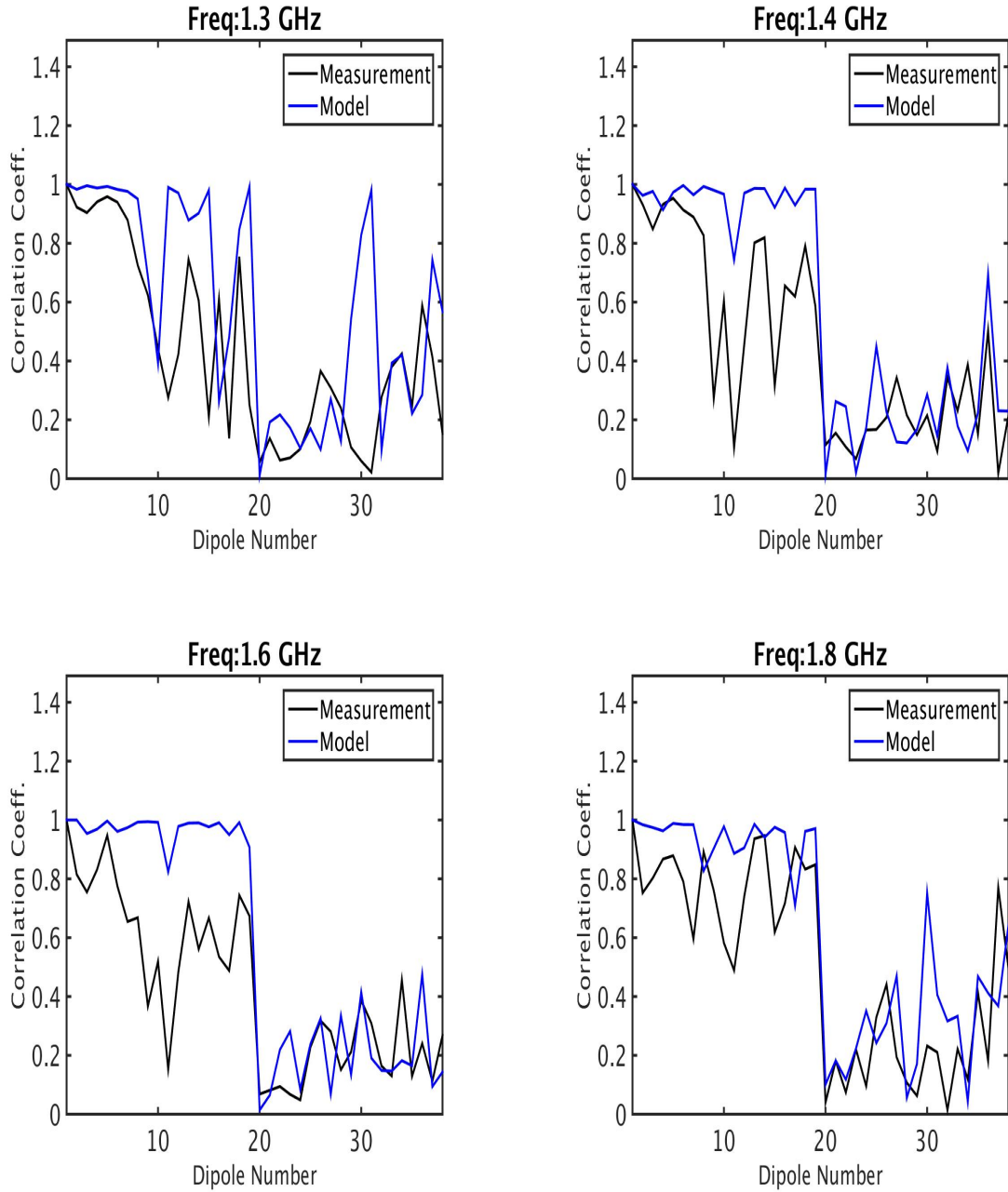


Figure 13: Model signal correlations (blue) and measured correlations due to source (black) between dipole1 and other dipoles. The measured signal correlations are obtained from the difference of on-source and off-source correlation matrices when the Virgo A is at the boresight. Dipoles 1 to 19 correspond to X polarization and dipoles 20 to 38 correspond to Y polarization.

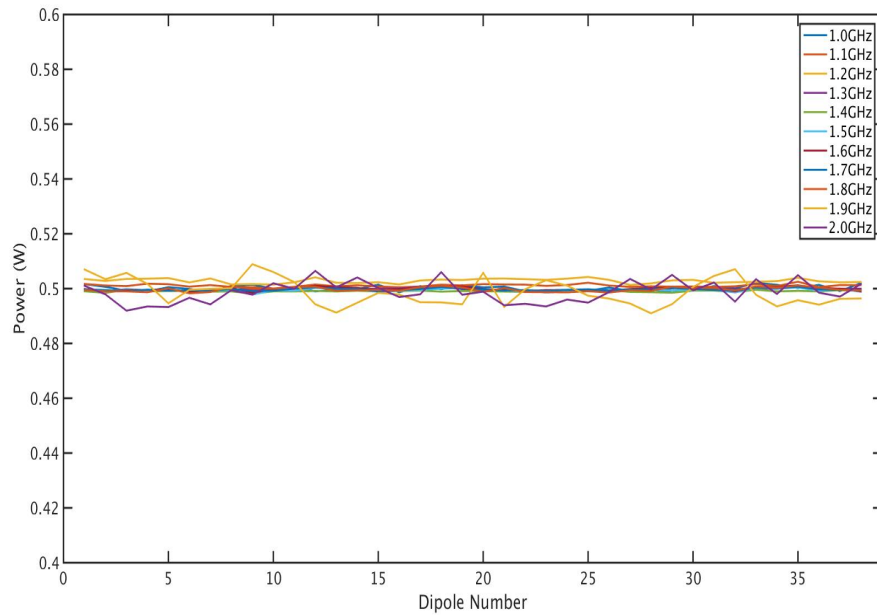


Figure 14: The sum of radiated and reflected power for different dipoles in the array. These powers are obtained using the Scattering matrix and radiation pattern provided by CST. The powers are computed for frequencies shown on the plot. As seen in the plot the sum of the radiated and reflected power is about 0.5 W, which is the RMS excitation power used by CST.

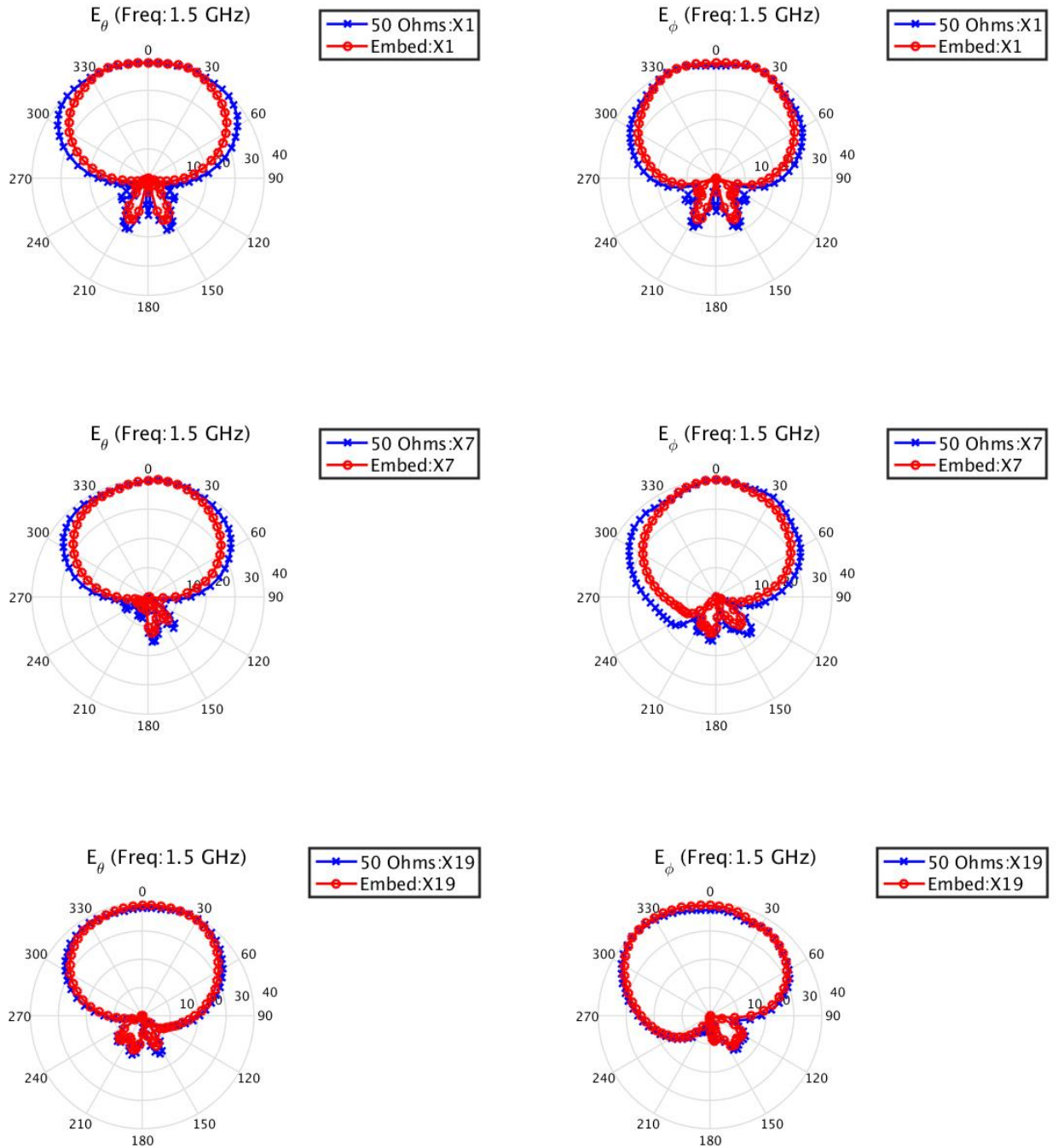


Figure 15: Plots of far-field pattern from the CST software package (blue) and the computed embedded beam patterns at 1.5 GHz (red).

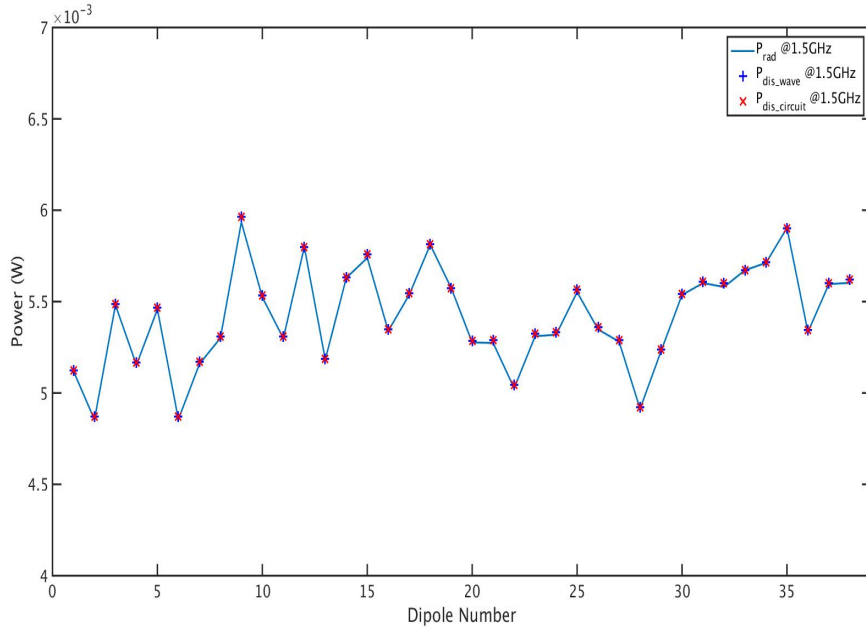


Figure 16: The radiated power computed with embedded pattern is compared with power dissipated at the excitation port. The dissipated powers are computed using Eq. 120 (marked as P_{dis_wave}) and Eq. 121 (marked as $P_{dis_circuit}$). As seen in the figure the radiated power is equal to the dissipated power.

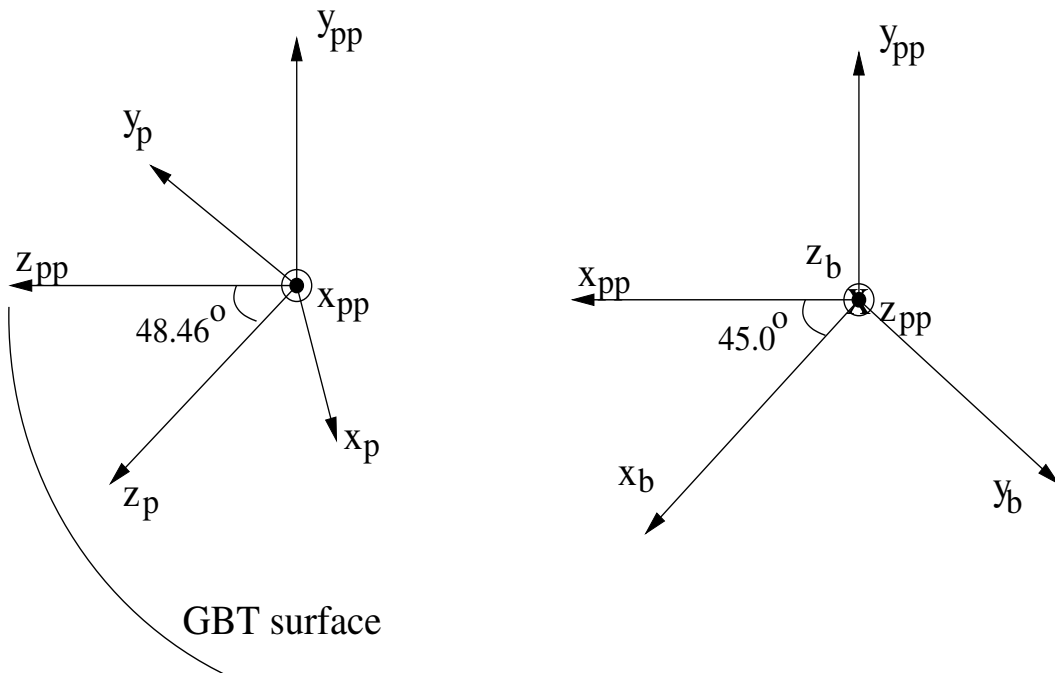


Figure 17: Coordinate system used for the computation of Eq. 51 and Eq. 54 (see text for details).